Alma Mater Studiorum · Università di Bologna

Scuola di Scienze
Dipartimento di Fisica e Astronomia
Corso di Laurea Magistrale in Fisica

Measurement of y_{CP} with D^0 mesons from semileptonic B-meson decays at LHCb

Relatore:

Prof. Angelo Carbone

Correlatori:

Dott. Federico Betti
Dott. Lorenzo Capriotti

Presentata da:

Andrea Villa

Anno Accademico 2019/2020

Abstract

This thesis reports a measurement of the charm-mixing observable y_{CP} using $D^0 \to K^+K^-$, $D^0 \to \pi^+\pi^-$, and $D^0 \to K^-\pi^+$ decays, where the D^0 meson originates from semileptonic B decays. The analysis is performed on the full Run 2 dataset collected by LHCb with pp collisions at a centre-of-mass energy of 13 TeV, corresponding to an integrated luminosity of $5.57\,\text{fb}^{-1}$.

The dataset is divided into 18 exclusive D^0 decay-time bins, in which an invariant mass fit is performed to extract the signal yield for each decay channel. The ratios of $KK/K\pi$ and $\pi\pi/K\pi$ yields in each bin, corrected for the decay-time acceptances estimated from a Monte Carlo sample, are then fitted to extract the difference between the decay widths of KK ($\pi\pi$) and $K\pi$ channels, $\Delta\Gamma^{KK}$ ($\Delta\Gamma^{\pi\pi}$).

Finally, y_{CP} is computed as $\Delta\Gamma\tau_{D^0}$, where τ_{D^0} is the precisely known D^0 lifetime. The values obtained from the two decay channels with preliminary systematic uncertainties are

$$y_{CP}^{KK} = (75.98 \pm 0.07\ (\text{stat}) \pm 0.06\ (\text{syst}))\,\%,$$
$$y_{CP}^{\pi\pi} = (76.29 \pm 0.14\ (\text{stat}) \pm 0.05\ (\text{syst}))\,\%,$$

which are consistent with each other (the central values are blind), and when combined yield a result of

$$y_{CP} = (76.08 \pm 0.06\ (\text{stat}) \pm 0.04\ (\text{syst}))\,\%.$$

The analysis aims at updating the previous LHCb measurement with a larger data sample size, and is expected to improve the precision by a factor two with respect to the current world average $y_{CP} = (0.715 \pm 0.111)\,\%$.

Sommario

In questa tesi si riporta una misura del parametro di mixing y_{CP} tramite lo studio dei decadimenti $D^0 \to K^+K^-$, $D^0 \to \pi^+\pi^-$, e $D^0 \to K^-\pi^+$, in cui il mesone D^0 ha origine da un decadimento semileptonico di un mesone B. L'analisi è compiuta sull'intero campione collezionato da LHCb durante il Run 2 con collisioni pp a una energia nel centro di massa di 13 TeV, corrispondenti a una luminosità integrata di $5.57\,\text{fb}^{-1}$.

Il campione di dati è suddiviso in 18 bin di tempo di decadimento del mesone D^0, in ciascuno dei quali è compiuto un fit alla distribuzione di massa invariante per estrarre il numero di eventi di segnale per ogni canale di decadimento. I rapporti tra il numero di eventi $KK/K\pi$ e $\pi\pi/K\pi$ in ogni bin, corretti con i rapporti di accettanze stimate con campioni Monte Carlo, sono poi fittati per estrarre le differenze tra le larghezze di decadimento dei canali KK ($\pi\pi$) e $K\pi$, Δ_Γ^{KK} ($\Delta_\Gamma^{\pi\pi}$).

Infine, y_{CP} è calcolato come $\Delta_\Gamma \tau_{D^0}$, dove τ_{D^0} è la vita media del mesone D^0, nota con precisione. I valori ottenuti nei due canali di decadimento con incertezze sistematiche preliminari sono

$$y_{CP}^{KK} = (75.98 \pm 0.07\ (\text{stat}) \pm 0.06\ (\text{syst}))\,\%,$$
$$y_{CP}^{\pi\pi} = (76.29 \pm 0.14\ (\text{stat}) \pm 0.05\ (\text{syst}))\,\%,$$

che sono reciprocamente consistenti (i valori centrali sono mascherati), e una volta combinati danno come risultato

$$y_{CP} = (76.08 \pm 0.06\ (\text{stat}) \pm 0.04\ (\text{syst}))\,\%.$$

Questa analisi, che intende aggiornare il precedente risultato di LHCb con un campione di dati più esteso, si prevede in grado di raggiungere una precisione di un fattore due migliore della attuale media mondiale, $y_{CP} = (0.715 \pm 0.111)\,\%$.

Contents

Introduction

Our current knowledge about three of the four fundamental forces (the electromagnetic, weak, and strong interactions) is formalised by the Standard Model, a theoretical framework that describes the kinematics and interactions between elementary particles. In a time span of around a century, the Standard Model has been established as one of the most precise theories ever formulated, with an incredible amount of predictions that were systematically confirmed by experimental tests.

The latest and most challenging success of the Standard Model has been the discovery of the Higgs boson, announced in 2012 by the CMS and ATLAS experiments [1, 2]. Thanks to this effort, the missing piece of the Standard Model has been found 48 years after the prediction of its existence.

Nonetheless, the Standard Model is far from being complete, since there are still many open questions: the origin of the observed matter-antimatter asymmetry in the universe; the fine tuning of the mass of the Higgs boson and other free parameters of the Standard Model; the nature of Dark Matter and Dark Energy; the incompatibility with the theory of General Relativity, which describes the gravitational force, and many others. All these questions suggest that the Standard Model is an incomplete theory, although a very precise one, and more experiments need to be carried out in order to shed some light on these unanswered problems.

The origin of the baryon asymmetry in the Universe is addressed by studying the decay and kinematics of hadrons containing the heavy quarks b and c and CP violation. The LHCb experiment is one of the world's leaders in this field, and in the past years has performed very precise measurements of CP violation in beauty and charm hadrons, rare decays branching ratios, discoveries of new baryons and exotic states, and so on.

The subject of this thesis is the search for CP violation in the charm sector, a phenomenon that was observed only very recently and therefore requires further studies and measurements to be understood in detail. In this document, a measurement of the charm-mixing observable y_{CP} will be presented; the analysis exploits LHCb's large dataset of $D^0 \to K^+K^-$, $D^0 \to \pi^+\pi^-$, and

$D^0 \to K^-\pi^+$ decays collected during Run 2 with pp collisions at a centre-of-mass energy of $\sqrt{s} = 13\,\text{TeV}$. This measurement aims at updating the previous LHCb result, and its precision is expected to be improved by a factor of 2.

The thesis is structured as follows:

- Chapter 1 presents an introduction to the Standard Model and the theoretical aspects of neutral mesons mixing and CP violation;
- In Chapter 2 the LHCb apparatus, with the sequence of specialised subdetectors needed to measure the many properties of particles coming from the collision, is described;
- Chapter 3 reports the description of the analysis process, the definition of the dataset used, the results of the measurement, and a preliminary study of systematic effects.

Chapter 1

Theory of charm mixing and *CP* violation

1.1 The Standard Model

The Standard Model (SM) is a non-abelian, locally gauge-invariant quantum field theory which describes three of the four fundamental forces of nature, namely the electromagnetic, strong, and weak interactions, together with the kinematic of free particles. The gravitational force is not included in the SM.

The Standard Model is described by the symmetry group

$$\mathrm{G_{SM}} = \mathrm{SU}(3)_C \times \mathrm{SU}(2)_L \times \mathrm{U}(1)_Y, \tag{1.1}$$

where $\mathrm{SU}(3)_C$ is the group upon which the description of strong interactions is based, and $\mathrm{SU}(2)_L \times \mathrm{U}(1)_Y$ is the group that rules the electromagnetic and weak interactions, unified through the Glashow–Weinberg–Salam (GWS) model [3–5]; the subscripts C, L, and Y indicate respectively the *colour*, the *chirality*, and the *hypercharge*.

In the Standard Model fundamental forces are mediated by elementary particles called *bosons*. All bosons are identified by an integer value of the spin quantum number, and are composed of the Higgs (the only one with spin 0), the photon, the gluons, and the weak carriers Z^0 and $W^\pm$ (all with spin 1).

The remaining elementary particles constitute the *fermions*, which all have a half-integer spin and are further divided into *leptons* and *quarks*, both grouped into three distinct generations or families. Each generation of quarks is made of four fields, two of which (left-handed quarks) are grouped together into a chirality doublet; the same applies to leptons, leading to a total of 6

Table 1.1: Quantum numbers of the six fermion fields: available colour charges, third component of the weak isospin (T_3), weak hypercharge (Y), and electric charge ($Q = T_3 + Y/2$).

	Field	Colours	T_3	Y	Q
Quarks	$Q_{L,i} = \begin{pmatrix} u_{L,i} \\ d_{L,i} \end{pmatrix}$	3	$\begin{pmatrix} 1/2 \\ -1/2 \end{pmatrix}$	$1/3$	$\begin{pmatrix} 2/3 \\ -1/3 \end{pmatrix}$
	$u_{R,i}$	3	0	$1/3$	$2/3$
	$d_{R,i}$	3	0	$-2/3$	$-1/3$
Leptons	$L_{L,i} = \begin{pmatrix} \nu_{L,i} \\ \ell_{L,i} \end{pmatrix}$	0	$\begin{pmatrix} 1/2 \\ -1/2 \end{pmatrix}$	-1	$\begin{pmatrix} 0 \\ -1 \end{pmatrix}$
	$\nu_{R,i}$	0	0	0	0
	$\ell_{R,i}$	0	0	-2	-1

distinct field multiplets:

$$Q_{L,i}, \quad u_{R,i}, \quad d_{R,i}, \quad L_{L,i}, \quad \ell_{R,i}, \quad \nu_{R,i}, \tag{1.2}$$

where the index $i = 1, 2, 3$ represents the family number, while L and R identify the left and right chirality. The quantum numbers of these fermions are reported in Tab. 1.1. Since right-handed neutrinos have all gauge charges equal to zero, they do not couple to any gauge boson, therefore their existence cannot be proved via Standard Model processes.

The Standard Model Lagrangian $\mathcal{L}_{\text{SM}}$ is the most general renormalisable Lagrangian that is consistent with the gauge symmetry of Eq. (1.1) and the particle content of Eq. (1.2), and it can be written as [6]

$$\mathcal{L}_{\text{SM}} = \mathcal{L}_g + \mathcal{L}_f + \mathcal{L}_H + \mathcal{L}_Y, \tag{1.3}$$

where $\mathcal{L}_g$ contains the kinetic and interaction terms between the gauge bosons, $\mathcal{L}_f$ the kinetic and interaction term for the fermions, $\mathcal{L}_H$ is the Higgs term, and $\mathcal{L}_Y$ is the Yukawa term responsible for the masses of the fermions.

To describe the four contributions we have to introduce the gauge fields G_a^μ (the eight gluons), W_b^μ (the three weak bosons), and B^μ (the hypercharge boson), together with three coupling constants g, g_s, and g'. We can then write the gauge term in Eq. (1.3) as:

$$\mathcal{L}_g = -\frac{1}{4}\left(G^a_{\mu\nu}G_a^{\mu\nu} + W^b_{\mu\nu}W_b^{\mu\nu} + B_{\mu\nu}B^{\mu\nu}\right), \tag{1.4}$$

where

$$B_{\mu\nu} = \partial_\mu B_\nu - \partial_\nu B_\mu, \tag{1.5a}$$
$$W^b_{\mu\nu} = \partial_\mu W^b_\nu - \partial_\nu W^b_\nu - g\varepsilon^b{}_{jk} W^j_\mu W^k_\nu, \tag{1.5b}$$
$$G^a_{\mu\nu} = \partial_\mu G^a_\nu - \partial_\nu G^a_\mu - g_s f^a{}_{jk} G^j_\mu G^k_\nu, \tag{1.5c}$$

are the field strength tensors. The symbols $\varepsilon^b{}_{jk}$ and $f^a{}_{jk}$ are the $\mathrm{SU}(2)_L$ and $\mathrm{SU}(3)_C$ structure constants, respectively.

The fermionic term, $\mathcal{L}_f$, can be written as

$$\mathcal{L}_f = \sum_{\text{fields}} i\overline{\psi}\gamma_\mu D^\mu \psi, \tag{1.6}$$

where γ_μ are the Dirac matrices, ψ and its adjoint $\overline{\psi} = \psi^\dagger\gamma^0$ represent one of the fields in Eq. (1.2), and D^μ is the covariant derivative that maintains gauge invariance, defined as

$$D^\mu = \partial^\mu + ig_s G^\mu_a L^a + igW^\mu_b T^b + ig' B^\mu Y, \tag{1.7}$$

where

- L_a are the $\mathrm{SU}(3)_C$ group generators, equal to the 3×3 Gell-Mann matrices $\lambda_a/2$ for colour triplets and to 0 for singlets; a goes from 1 to 8;
- T_b are the $\mathrm{SU}(2)_L$ group generators, equal to the 2×2 Pauli matrices $\sigma_b/2$ for isospin doublets and to 0 for singlets; b goes from 1 to 3;
- Y is the $\mathrm{U}(1)_Y$ group generator, equal to the hypercharge of each particle as reported in Tab. 1.1.

Next, the Higgs term in the Lagrangian has the form

$$\mathcal{L}_H = (D^\mu\phi^\dagger)(D_\mu\phi) + \mu^2\phi^\dagger\phi - \frac{\lambda^2}{2}\left(\phi^\dagger\phi\right)^2, \tag{1.8}$$

with λ and $\mu = v\sqrt{\lambda}$ real and positive parameters. The Higgs field ϕ can be written as an isospin doublet with hypercharge 1, $\phi = (\phi^+, \phi^0)^T$, which assumes a non-zero vacuum expectation value

$$\langle\phi\rangle = \frac{1}{\sqrt{2}}\begin{pmatrix}0\\ v\end{pmatrix}, \tag{1.9}$$

with $v \simeq 246\,\mathrm{GeV}$; this causes the symmetry with respect to $\mathrm{SU}(2)_L \times \mathrm{U}(1)_Y$ to be spontaneously broken, so that the gauge group $\mathrm{G_{SM}}$ collapses to $\mathrm{SU}(3)_C \times \mathrm{U}(1)_{\mathrm{EM}}$.

The Yukawa term in the Lagrangian describes the interaction between fermions and the scalar Higgs field and reads as follow:

$$\mathcal{L}_Y = -Y^d_{ij}\overline{Q}_{L,i}\phi d_{R,j} - Y^u_{ij}\overline{Q}_{L,i}(i\sigma_2\phi^\dagger)u_{R,j} - Y^\ell_{ij}\overline{L}_{L,i}\phi\ell_{R,j} + h.c., \tag{1.10}$$

where *h.c.* stands for *hermitian conjugates* and the Y^f_{ij} are general 3×3 complex matrices that couple the fermion fields to the Higgs field. After the spontaneous breaking of the electroweak symmetry and given the nonzero vacuum expectation value of the Higgs field (Eq. (1.9)), replacing $\mathfrak{Re}(\phi^0)$ with $(v + H)/\sqrt{2}$, where H is the Higgs boson, gives the Yukawa mass terms

$$\mathcal{L}_Y = -M^d_{ij}\overline{d}_{L,i}d_{R,j} - M^u_{ij}\overline{u}_{L,i}u_{R,j} - M^\ell_{ij}\overline{\ell}_{L,i}\ell_{R,j} + h.c., \tag{1.11}$$

where $M^f_{ij} = vY^f_{ij}/\sqrt{2}$ are the fermionic mass matrices. Note that since neutrinos do not have Yukawa couplings, they are predicted to be massless[1].

The quark fields d_i and u_i do not correspond to the physical states observed experimentally, because the matrices M^d_{ij} and M^u_{ij} are not diagonal. To describe physical processes, we have to find the quark mass eigenstates, which can be done by diagonalising the mass matrices M^q_{ij}, with $q = (u, d)$; the two matrices can be diagonalised by finding four suitable unitary matrices V^q_L and V^q_R such that

$$V^q_L M^q (V^q_R)^\dagger = \mathcal{M}^q, \tag{1.12}$$

with

$$\mathcal{M}^u = \begin{pmatrix} m_u & 0 & 0 \\ 0 & m_c & 0 \\ 0 & 0 & m_t \end{pmatrix}, \quad \mathcal{M}^d = \begin{pmatrix} m_d & 0 & 0 \\ 0 & m_s & 0 \\ 0 & 0 & m_b \end{pmatrix}. \tag{1.13}$$

We can now write the quark mass eigenstates as

$$q_{L,i} = (V^q_L)_{ij} q_{L,j}, \qquad q_{R,i} = (V^q_R)_{ij} q_{R,j}, \tag{1.14}$$

so that the Yukawa term (1.11) becomes (for quarks only):

$$\mathcal{L}_Y = -\mathcal{M}^d_{ij}\overline{d}_{L,i}d_{R,j} - \mathcal{M}^u_{ij}\overline{u}_{L,i}u_{R,j} + h.c. \tag{1.15}$$

1.2 Charge and parity conjugation

The subject of this thesis is the violation of the symmetry that combines charge (C) and parity (P) conjugation, namely *CP* symmetry. This transformation

[1] This is in contrast with the recent observation of the phenomenon of *neutrino oscillation* [7], in which neutrinos are found to change flavour during their lifetime. This can happen only if all three neutrinos have non-vanishing mass.

plays an important role in the Standard Model because its violation is one of the Sakharov conditions for baryogenesis in the universe [8]. Moreover, the violation of CP symmetry by the weak interaction allows for the occurrence of particle decays that would otherwise be forbidden, like $K_L^0 \to \pi^+\pi^-$.

The charge conjugation transformation is realised by an operator that flips the sign of the charge [9]:

$$\hat{C}^\dagger \hat{Q} \hat{C} = -\hat{Q}, \tag{1.16}$$

where Q identifies not only the electric charge, but all the charges responsible for couplings to the gauge bosons. Charge conjugation acts on a state with momentum $\vec{p}$, spin s and charge q as

$$\hat{C} \left|\vec{p}, s, q\right\rangle = \eta_C \left|\vec{p}, s, -q\right\rangle, \tag{1.17}$$

meaning that the chirality of the particle is conserved by the transformation. Since two successive iterations of the charge conjugation must transform a particle back to itself, the eigenvalue η_C, called charge conjugation parity or C-parity, can only take values ± 1 for an eigenstate of the transformation.

C-parity is a multiplicative quantity, meaning that a system composed of several particles, which are charge-conjugation eigenstates, has a C-parity given by the product of the single eigenvalues for each particle.

The parity transformation is defined as the inversion of the spatial coordinates of a system, so that its effect on a particle field can be written as

$$\hat{P}^\dagger \phi(\vec{x}, t) \hat{P} = \eta_P \phi(-\vec{x}, t), \tag{1.18}$$

where the parity eigenvalue, η_P, like C-parity can only take values ± 1, and is also a multiplicative quantity. A parity transformation leaves untouched the spin of a particle while reversing its momentum, so that the chirality of the particle is flipped by the transformation.

A system is symmetric with respect to charge and parity conjugation if the respective operators commute with the Hamiltonian H,

$$\left[\hat{H}, \hat{C}\right] = 0, \quad \left[\hat{H}, \hat{P}\right] = 0. \tag{1.19}$$

Historically, for a long time parity was believed to be a valid symmetry for all the fundamental interactions described by the Standard Model, until a careful review showed that while the electromagnetic and strong interactions were proven to be parity-conserving, the evidence for the conservation of parity by weak interactions was lacking [10]. Dedicated experiments were quickly set up to address the question, which showed for the first time that P-symmetry

is violated by the weak force by studying respectively polarised ^{60}Co nuclei and muons from charged pion decays [11, 12].

At first, the violation of both C- and P-symmetry led to believe that their combination, CP, would still be preserved by the weak interaction. This claim was also proved wrong less than a decade later, when Cronin, Fitch *et al.* observed the decay $K_L^0 \to \pi^+\pi^-$, which violates CP conservation [13].

1.3 The CKM matrix

The matrix

$$V_{CKM} = V_L^u (V_L^d)^\dagger = \begin{pmatrix} V_{ud} & V_{us} & V_{ub} \\ V_{cd} & V_{cs} & V_{cb} \\ V_{td} & V_{ts} & V_{tb} \end{pmatrix} \tag{1.20}$$

is a 3×3 unitary matrix called the *Cabibbo–Kobayashi–Maskawa* (CKM) quark mixing matrix [14, 15]. The squares of the elements of the matrix represent the probability of a transition between the respective quarks.

Any complex unitary matrix of dimension N can be parameterised by means of $N(N-1)/2$ rotation angles and $N(N+1)/2$ phases. Furthermore, not all the possible phase choices affect the Lagrangian, so that it is safe to exclude $2N-1$ of them, ending with a total of $(N-1)(N-2)/2$.

That means that the CKM matrix, with 3 generations of fermions, only needs 3 Euler angles and one phase as independent parameters, namely θ_{12}, θ_{23}, θ_{13}, and δ, which is responsible for CP violation in quark mixing.

With the notation $s_{ij} = \sin(\theta_{ij})$ and $c_{ij} = \cos(\theta_{ij})$, the matrix can be written as

$$V_{CKM} = \begin{pmatrix} c_{12}c_{13} & s_{12}c_{13} & s_{13}e^{-i\delta} \\ -s_{12}c_{23} - c_{12}s_{23}s_{13}e^{i\delta} & c_{12}c_{23} - s_{12}s_{23}s_{13}e^{i\delta} & s_{23}c_{13} \\ s_{12}s_{23} - c_{12}c_{23}s_{13}e^{i\delta} & -c_{12}s_{23} - s_{12}c_{23}s_{13}e^{i\delta} & c_{23}c_{13} \end{pmatrix}. \tag{1.21}$$

Even though the above representation is exact, a different parameterisation proves much more useful in understanding the hierarchy between the elements, the so-called Wolfenstein parameterisation [16], in which 4 different parameters (λ, A, ρ, η) are used, defined by the relations

$$\lambda = s_{12}, \quad A\lambda^2 = s_{23}, \quad A\lambda^3(\rho - i\eta) = s_{13}e^{-i\delta}. \tag{1.22}$$

With this transformation, the matrix is expressed as a power series in terms of $\lambda \approx 0.22$, which up to terms of order λ^3 reads as

$$V_{CKM} = \begin{pmatrix} 1 - \lambda^2/2 & \lambda & A\lambda^3(\rho - i\eta) \\ -\lambda & 1 - \lambda^2/2 & A\lambda^2 \\ A\lambda^3\,(1 - \rho - i\eta) & -A\lambda^2 & 1 \end{pmatrix} + \mathcal{O}\left(\lambda^4\right), \tag{1.23}$$

where it is evident how the diagonal elements of the matrix are close to 1, and how they get smaller the more off-diagonal they go. This means that transitions between same-family quark are favoured, while jumps of one family or more are suppressed.

This can also be observed by looking at the magnitudes of the elements of V_{CKM}, which to this day are estimated as follows [17]

$$|V_{CKM}| = \begin{pmatrix} 0.97446(10) & 0.22452(44) & 0.00365(12) \\ 0.22438(44) & 0.97359(^{+10}_{-11}) & 0.04214(76) \\ 0.00896(^{+24}_{-23}) & 0.04133(74) & 0.999105(32) \end{pmatrix}, \tag{1.24}$$

with the uncertainties inside brackets, of the same order of the least significant digits of the central value.

The parameterisation in Eq. (1.21) is not unique, since the CKM matrix is defined up to a global phase; nonetheless, it is possible to compute a *CP*-violating quantity which is independent of the parameterisation used, the Jarlskog invariant J_{CP}, defined through the relation [18]

$$\mathfrak{Im}\left(V_{ij}V_{kl}V_{il}^{*}V_{kj}^{*}\right) = J_{CP}\sum_{m,n=1}^{3}\varepsilon_{ikm}\varepsilon_{jln}, \quad i,j,k,l \in \{1,2,3\}, \tag{1.25}$$

where V_{CKM} was written as V for simplicity. J_{CP} can also be computed as

$$J_{CP} = s_{12}s_{13}s_{23}c_{12}c_{13}^{2}c_{23}\sin\delta. \tag{1.26}$$

It can be shown [19] that a necessary condition for the existence of *CP* violation due to quark mixing is the non-vanishing of

$$(m_t^2 - m_c^2)(m_t^2 - m_u^2)(m_c^2 - m_u^2)(m_b^2 - m_s^2)(m_b^2 - m_d^2)(m_s^2 - m_d^2)J_{CP}, \tag{1.27}$$

which, given the definition of J_{CP} in Eq. (1.26), implies that in order to have *CP* violation in the Standard Model, up- and down-quark masses should not be degenerate, the three mixing angles should not be equal to 0 or $\pi/2$, the phase should be neither 0 nor π, and $J_{CP} \neq 0$.

The existence of *CP* violation is well-established today, confirmed by the current value of $J_{CP} = (3.18 \pm 0.15) \times 10^{-5}$ [17]. A less abstract way to understand the role of *CP* violation in the quark sector is through the so-called *unitary triangles*; the unitarity of the CKM matrix ($VV^{\dagger} = 1$) implies a set of 9 equations of the form

$$\sum_{k\in\{u,c,t\}} V_{ki}V_{kj}^{*} = \delta_{ij}, \quad i,j \in \{d,s,b\}, \tag{1.28}$$

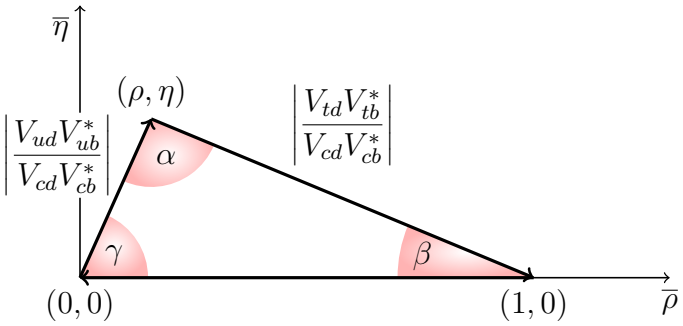

Figure 1.1: Unitary triangle from Eq. (1.29) in the $(\overline{\rho},\overline{\eta})$ plane.

6 of which require the sum of 3 complex quantities to vanish, and can therefore be represented as triangles in the complex plane, all with the same area $|J_{CP}|/2$. One in particular has been chosen for precision tests of the Standard Model:

$$\underbrace{V_{ud}V_{ub}^*}_{\mathcal{O}(\lambda^3)}+\underbrace{V_{cd}V_{cb}^*}_{\mathcal{O}(\lambda^3)}+\underbrace{V_{td}V_{tb}^*}_{\mathcal{O}(\lambda^3)}=0. \tag{1.29}$$

The triangle in Eq. (1.29) is shown in Fig. 1.1, after choosing a phase convention such that $V_{cd}V_{cb}^*$ is real and dividing every side by $|V_{cd}V_{cb}^*|$. This way two vertices of the triangle coincide with $(0,0)$ and $(1,0)$ and the coordinates of the third vertex correspond to the Wolfenstein parameters (ρ,η).

The three angles of the unitary triangle are called α, β, and γ and correspond to

$$\alpha=\arg\left(-\frac{V_{td}V_{tb}^*}{V_{ud}V_{ub}^*}\right),\quad \beta=\arg\left(-\frac{V_{cd}V_{cb}^*}{V_{td}V_{tb}^*}\right),\quad \gamma=\arg\left(-\frac{V_{ud}V_{ub}^*}{V_{cd}V_{cb}^*}\right). \tag{1.30}$$

The most recent experimental constraints on the unitary triangle parameters are shown in Fig. 1.2 in the $(\overline{\rho},\overline{\eta})$ plane.

1.4 Neutral mesons mixing phenomenology

We will now provide a phenomenological description of the mechanism of neutral mesons mixing, and its contribution to CP violation.

The formalism introduced below will be referring in particular to D^0 and $\overline{D^0}$ mesons, but it could be used as well to describe the mixing in other neutral mesons systems, such as K^0, B^0, and B_s^0, with different results due to mass, decay rates, and oscillation differences.

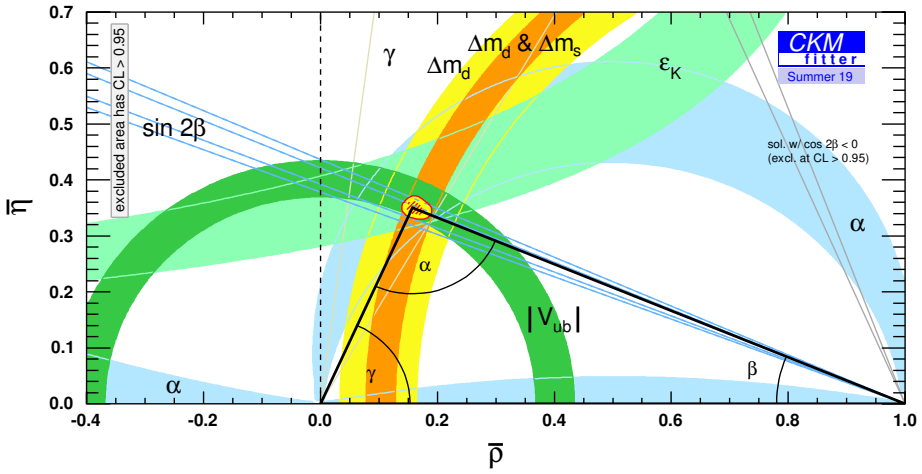

Figure 1.2: Current experimental knowledge of the parameters of the unitary triangle [20].

For a generic D meson (charged or neutral) and its CP-conjugate $\overline{D}$ the decay amplitudes into a multi-body final state f and its CP-conjugate $\overline{f}$ can be defined as

$$A_f = \langle f|\mathcal{H}|D\rangle\,, \quad A_{\overline{f}} = \left\langle \overline{f}\middle|\mathcal{H}\middle|D\right\rangle, \tag{1.31a}$$

$$\overline{A}_f = \left\langle f\middle|\mathcal{H}\middle|\overline{D}\right\rangle, \quad \overline{A}_{\overline{f}} = \left\langle \overline{f}\middle|\mathcal{H}\middle|\overline{D}\right\rangle, \tag{1.31b}$$

where $\mathcal{H}$ is the weak interaction Hamiltonian. Two types of phases can be included in these amplitudes, namely *weak* phases, coming from the couplings to the $W^{\pm}$ bosons, that affect the CP-conjugate amplitudes, and *strong* phases which arise from possible contributions of intermediate on-shell states mediated by the strong interaction, and therefore CP-invariant, meaning that they do not change between A_f and $\overline{A}_{\overline{f}}$.

CP violation can occur either because $|A_f| \neq \left|A_{\overline{f}}\right|$ or due to the oscillation between neutral meson flavours [21], which arises from the difference between the mass eigenstates and the flavour eigenstates that are experimentally detected. This difference causes an initially pure state, for example a D^0, to evolve in time into a linear combination of D^0 and $\overline{D^0}$ states, which after a time t much larger than the typical strong interaction timescale can be described by the Schrödinger equation

$$i\frac{\partial}{\partial t}\begin{pmatrix}\left|D^0(t)\right\rangle \\ \left|\overline{D^0}(t)\right\rangle\end{pmatrix} = \left(\mathbf{M} - \frac{i}{2}\mathbf{\Gamma}\right)\begin{pmatrix}\left|D^0(t)\right\rangle \\ \left|\overline{D^0}(t)\right\rangle\end{pmatrix}, \tag{1.32}$$

where $\mathbf{M}$ and $\mathbf{\Gamma}$ are 2×2 Hermitian matrices, for which *CPT* invariance implies $\mathbf{M}_{11} = \mathbf{M}_{22}$ and $\mathbf{\Gamma}_{11} = \mathbf{\Gamma}_{22}$.

The eigestates of the matrix $\mathbf{H} = \mathbf{M} - i\mathbf{\Gamma}/2$ are called D_H and D_L, to represent the heavy and light state, respectively. They can be written as:

$$|D_L\rangle = p\left|D^0\right\rangle + q\left|\overline{D^0}\right\rangle, \tag{1.33a}$$

$$|D_H\rangle = p\left|D^0\right\rangle - q\left|\overline{D^0}\right\rangle, \tag{1.33b}$$

where p and q are complex parameters with the properties $|p|^2 + |q|^2 = 1$ and $q/p = \sqrt{\mathbf{H}_{21}/\mathbf{H}_{12}}$. The corresponding eigenvalues $\lambda_{H,L}$ can be computed as

$$\lambda_{H,L} = \frac{\mathbf{H}_{11} + \mathbf{H}_{22}}{2} \mp \sqrt{\mathbf{H}_{12}\mathbf{H}_{21}} = m_{H,L} - \frac{i}{2}\Gamma_{H,L}, \tag{1.34}$$

with $m_{H,L}$ and $\Gamma_{H,L}$ the mass and width of the two states. We also define the average values and the differences between these two quantities as

$$m = (m_H + m_L)/2, \tag{1.35a}$$

$$\Gamma = (\Gamma_H + \Gamma_L)/2, \tag{1.35b}$$

$$\Delta m = m_H - m_L, \tag{1.35c}$$

$$\Delta\Gamma = \Gamma_H - \Gamma_L. \tag{1.35d}$$

While $\Delta m > 0$ by definition, the sign of $\Delta\Gamma$ is not predictable and must be determined experimentally.

We can now write the expression for the flavour mixture of an initially pure D^0 or $\overline{D^0}$ state at a generic time t:

$$|D(t)\rangle = g_+(t)\,|D\rangle + \frac{q}{p}g_-(t)\left|\overline{D^0}\right\rangle, \tag{1.36a}$$

$$\left|\overline{D^0}(t)\right\rangle = \frac{p}{q}g_-(t)\,|D\rangle + g_+(t)\left|\overline{D^0}\right\rangle, \tag{1.36b}$$

where

$$g_\pm(t) = \frac{1}{2}\left(e^{-i\lambda_L t} \pm e^{-i\lambda_H t}\right). \tag{1.37}$$

If we define the adimensional mixing parameters x and y as

$$x = \frac{\Delta m}{\Gamma}, \qquad y = \frac{\Delta\Gamma}{2\Gamma}, \tag{1.38}$$

we can write for the squared magnitude of the functions in Eq. (1.37)

$$|g_\pm(t)|^2 = \frac{e^{-\Gamma t}}{2}\left[\cosh(y\Gamma t) \pm \cos(x\Gamma t)\right]. \tag{1.39}$$

Table 1.2: Approximate values of x and y of the four oscillating neutral mesons [22].

	$x = \Delta m/\Gamma$	$y = \Delta\Gamma/2\Gamma$
$K^0 - \overline{K^0}$	-0.95	0.997
$D^0 - \overline{D^0}$	0.004	0.007
$B^0 - \overline{B^0}$	0.76	0.0005
$B_s^0 - \overline{B_s^0}$	26.8	0.07

It is easy to obtain the time-dependent decay rate of a D meson into a generic f state by simply multiplying $\langle f|$ or $\left\langle \overline{f} \right|$ to one of the two in Eqs. (1.33a) and (1.33b). For example, the decay rate of $D^0 \to f$ is explicitly written as

$$\Gamma\left(D^0 \to f; t\right) = \left| g_+(t) \left\langle f \middle| \mathcal{H} \middle| D^0 \right\rangle + \frac{q}{p} g_-(t) \left\langle f \middle| \mathcal{H} \middle| \overline{D^0} \right\rangle \right|^2 \tag{1.40}$$

$$= |A_f|^2 \left| g_+(t) + \lambda_f g_-(t) \right|^2, \tag{1.41}$$

with

$$\lambda_f = \frac{q}{p} \frac{\overline{A}_f}{A_f}, \tag{1.42}$$

and similarly for the other combinations. With the same approach we can easily compute the probability of a D^0 meson to maintain its flavour content at a time t or to oscillate into its antiparticle $\overline{D^0}$:

$$P\left(D^0 \to D^0; t\right) = \left\langle D^0 \middle| D^0(t) \right\rangle = |g_+(t)|^2, \tag{1.43a}$$

$$P\left(D^0 \to \overline{D^0}; t\right) = \left\langle \overline{D^0} \middle| D^0(t) \right\rangle = |q/p|^2 |g_-(t)|^2. \tag{1.43b}$$

These oscillation probabilities are plotted in Fig. 1.3 for the four neutral meson systems K^0-$\overline{K^0}$, D^0-$\overline{D^0}$, B^0-$\overline{B^0}$, and B_s^0-$\overline{B_s^0}$, whose values of x and y are reported in Tab. 1.2.

1.5 Mechanisms of CP violation and the parameter y_{CP}

The possibility for a neutral meson to oscillate between two distinct flavours provides additional ways to violate the CP symmetry, which can be classified as:

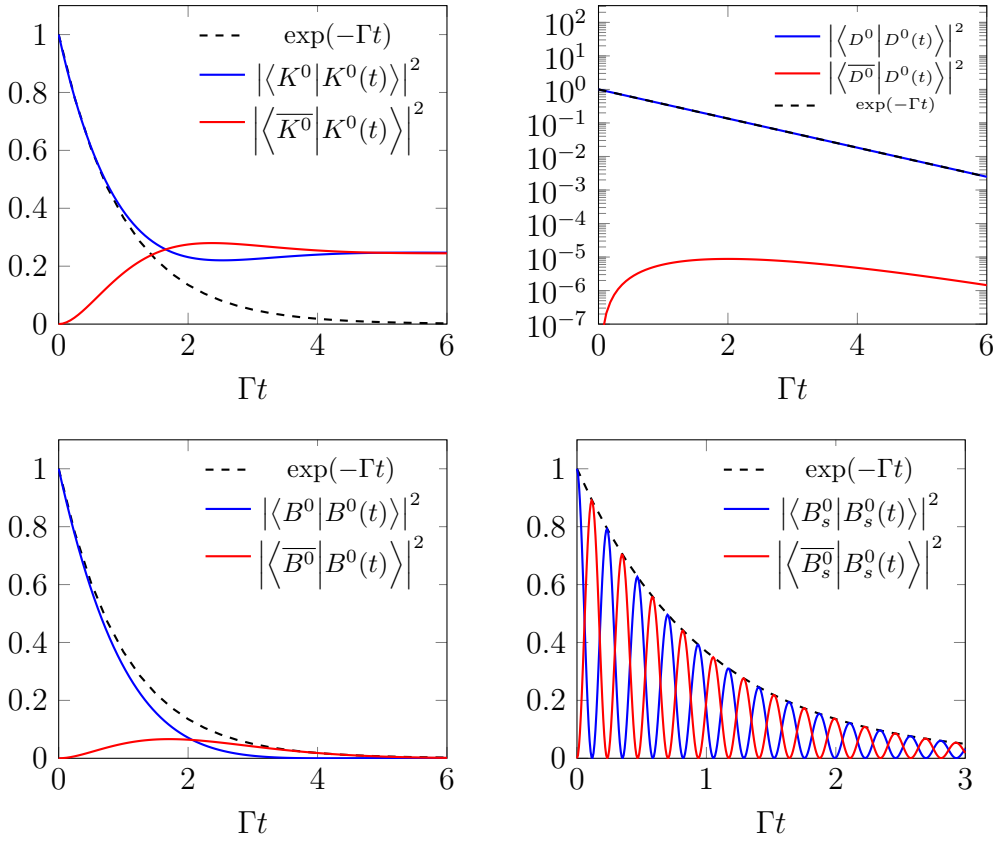

Figure 1.3: Oscillation probabilities as a function of time (in units of the mean lifetime) for the four neutral mesons K^0-$\overline{K^0}$, D^0-$\overline{D^0}$, B^0-$\overline{B^0}$, and B_s^0-$\overline{B_s^0}$.

1. *CP* violation in the decay, occurring if $\left|A_f/\overline{A}_{\overline{f}}\right| \neq 1$, that is also possible for charged mesons. It can be studied with the asymmetry observable

$$A_{CP}(f) = \frac{\Gamma(D^0 \to f) - \Gamma(\overline{D^0} \to \overline{f})}{\Gamma(D^0 \to f) + \Gamma(\overline{D^0} \to \overline{f})} = \frac{1 - \left|\overline{A}_{\overline{f}}/A_f\right|^2}{1 + \left|\overline{A}_{\overline{f}}/A_f\right|^2}. \tag{1.44}$$

   For the condition $|A_f| \neq \left|\overline{A}_{\overline{f}}\right|$ to be satisfied at least two terms in the amplitudes must have different strong and weak phases. For example, if an amplitude is made up of several contributions such as

$$A_f = \sum_k |A_k| e^{i(\delta_k + \phi_k)}, \tag{1.45}$$

   where $|A_k|$, δ_k, and ϕ_k are the magnitude, strong phase and weak phase of the k-th contribution respectively, then the difference between the squared amplitudes $|A_f|^2$ and $\left|\overline{A}_{\overline{f}}\right|^2$ is

$$|A_f|^2 - \left|\overline{A}_{\overline{f}}\right|^2 = -2 \sum_{k,j} |A_k||A_j| \sin(\delta_k - \delta_j) \sin(\phi_k - \phi_j); \tag{1.46}$$

2. *CP* violation in mixing, defined by the relation $|q/p| \neq 1$, which can be observed through the time-dependent version of Eq. (1.44),

$$A_{CP}(f;t) = \frac{\mathrm{d}\Gamma(D^0(t) \to f)/\,\mathrm{d}t - \mathrm{d}\Gamma(\overline{D^0}(t) \to \overline{f})/\,\mathrm{d}t}{\mathrm{d}\Gamma(D^0(t) \to f)/\,\mathrm{d}t + \mathrm{d}\Gamma(\overline{D^0}(t) \to \overline{f})/\,\mathrm{d}t}; \tag{1.47}$$

3. *CP* violation in the interference between mixing and decay, only possible if the final state f is common to both D^0 and $\overline{D^0}$ and when $\mathfrak{Im}(\lambda_f) \neq 0$. It is to be noted that due to the interference term, *CP* violation can occur even when $\left|A_f/\overline{A}_{\overline{f}}\right| = 1$ and $|q/p| = 1$.

Type 1 is usually referred to as *direct CP* violation, while types 2 and 3 are known as *indirect CP* violation. To this day, *CP* violation as been observed, either directly or indirectly, in all four oscillating neutral meson systems [23–27].

The presence of mixing modifies the time dependence of the decay rates $D^0 \to f$ from a pure exponential, as shown in Eq. (1.40). However, given the small values of x and y (Tab. 1.2), the exponential form can be approximately restored with effective decay widths

$$\hat{\Gamma} = \Gamma \left[1 + \eta_{CP} \left|\frac{q}{p}\right| \left|\frac{\overline{A}_f}{A_f}\right| (y \cos\phi_D - x \sin\phi_D)\right], \tag{1.48a}$$

$$\hat{\overline{\Gamma}} = \Gamma \left[1 + \eta_{CP} \left|\frac{q}{p}\right| \left|\frac{\overline{A}_f}{A_f}\right| (y \cos\phi_D + x \sin\phi_D)\right], \tag{1.48b}$$

with η_{CP} the *CP* eigenvalue of the final state and $\phi_D = \arg\left(q\overline{A}_f/pA_f\right)$. From these is possible to define two useful *CP* observables (considering *CP*-even final states such as K^+K^- and $\pi^+\pi^-$, for which $\eta_{CP} = 1$ and $\left|\overline{A}_f/A_f\right| = 1$):

$$y_{CP} = \frac{\hat{\overline{\Gamma}} + \hat{\Gamma}}{2\Gamma} - 1 \tag{1.49a}$$

$$= \frac{1}{2}\left[\left(\left|\frac{q}{p}\right| + \left|\frac{p}{q}\right|\right) y\cos\phi_D - \left(\left|\frac{q}{p}\right| - \left|\frac{p}{q}\right|\right) x\sin\phi_D\right], \tag{1.49b}$$

$$A_\Gamma = \frac{\hat{\Gamma} - \hat{\overline{\Gamma}}}{2\Gamma} \tag{1.49c}$$

$$= \frac{1}{2}\left[\left(\left|\frac{q}{p}\right| - \left|\frac{p}{q}\right|\right) y\cos\phi_D - \left(\left|\frac{q}{p}\right| + \left|\frac{p}{q}\right|\right) x\sin\phi_D\right], \tag{1.49d}$$

$$\tag{1.49e}$$

which in the limit of *CP* conservation are expected to be $y_{CP} = y$ and $A_\Gamma = 0$, meaning that a significant deviation from these values would imply *CP* violation.

Regarding y_{CP}, which is the observable measured in this analysis, the current experimental knowledge is summarised in Fig. 1.4. The most precise measurements come from the experiments BaBar, Belle, and LHCb [28–30].

The Heavy FLavour AVeraging group (HFLAV [22]) periodically computes the world averages of the available measurements of many observables from beauty and charm physics; their latest result for y_{CP} is the value $y_{CP} = (0.715 \pm 0.111)\,\%$. The group also performs a global fit, using as inputs many different results and average values of charm mixing observables, to obtain the most precise estimate of y, namely $y = (0.651^{+0.063}_{-0.069})\%$; this value is compatible with the average value of y_{CP}, meaning that no evidence of indirect *CP* violation is present to this day.

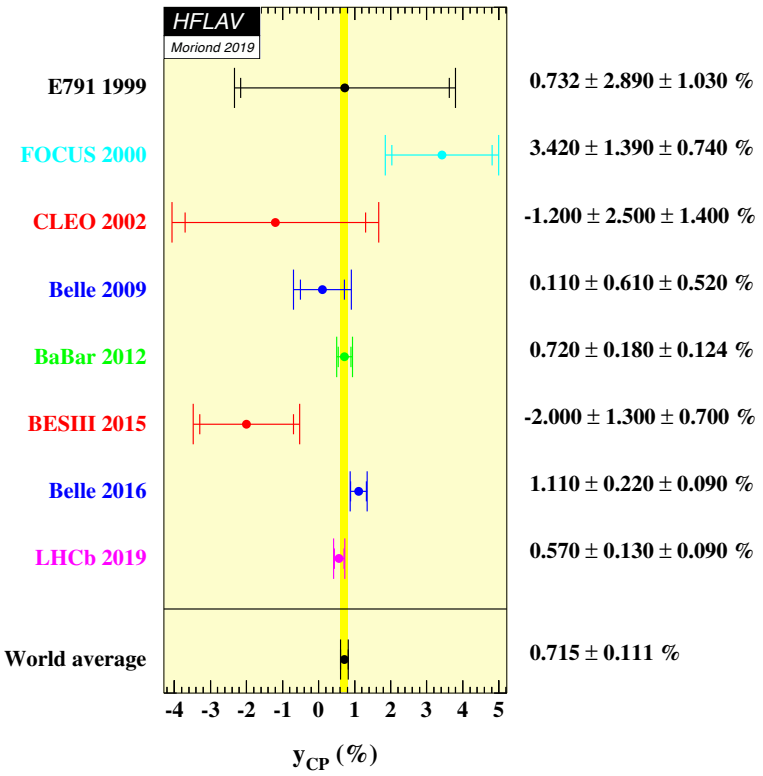

Figure 1.4: Overview of the past measurements of the y_{CP} observable and their average [22].

Chapter 2

The LHCb detector at the LHC

In this chapter the LHCb detector, one of the four main experiments installed at the Large Hadron Collider (LHC), is presented. The sub-detectors systems are briefly described and the reconstruction and data acquisition performances are reported relatively to the data-taking campaign relevant to this analysis (Run 2).

2.1 The LHC accelerator

The Large Hadron Collider [31], located 100 m underground across the border between France and Switzerland, in the tunnel that previously hosted the electron-positron collider LEP, is currently the world's largest particle accelerator, being capable of colliding protons at a centre-of-mass energy of 13 TeV and lead ions up to 2.76 TeV per nucleon.

LHC is a two-ring circular collider with a diameter of 26.7 km, designed to achieve an instantaneous luminosity of $10^{34}\,\mathrm{cm}^{-2}\,\mathrm{s}^{-1}$. To reach this goal, proton beams are accelerated by superconducting multipole magnets with a magnetic field intensity of 8.3 T, cooled with superfluid helium down to a temperature of 1.9 K.

LHC is the final stage in a long chain of accelerator systems, starting with a linear accelerator (LINAC-2) which pushes the protons from rest up to an energy of 50 MeV, then passing through a proton synchrotron Booster (BOOSTER) that increases their energy to 1.5 GeV. From this point, protons enter the Proton Synchrotron (PS) to reach an energy of 25 GeV, and a Super Proton Synchrotron (SPS) that accelerates them to 450 GeV, from which they finally get injected into LHC to reach the maximum energy. A complete picture of the LHC injection system is shown in Fig. 2.1.

Inside the beam tubes, protons are grouped in 2808 bunches of around

10^{11} particles that collide at a 40 MHz rate in 4 four interaction points along the circumference, where the 4 main experiments of LHC are installed, namely ALICE, ATLAS, CMS, and LHCb.

During the first data-taking campaign (Run 1), LHC collided protons at a centre-of-mass energy $\sqrt{s} = 7$ and 8 TeV in 2011 and 2012, respectively. In the following campaign (RUN-2), spanning from 2015 to 2018, the energy was increased to 13 TeV.

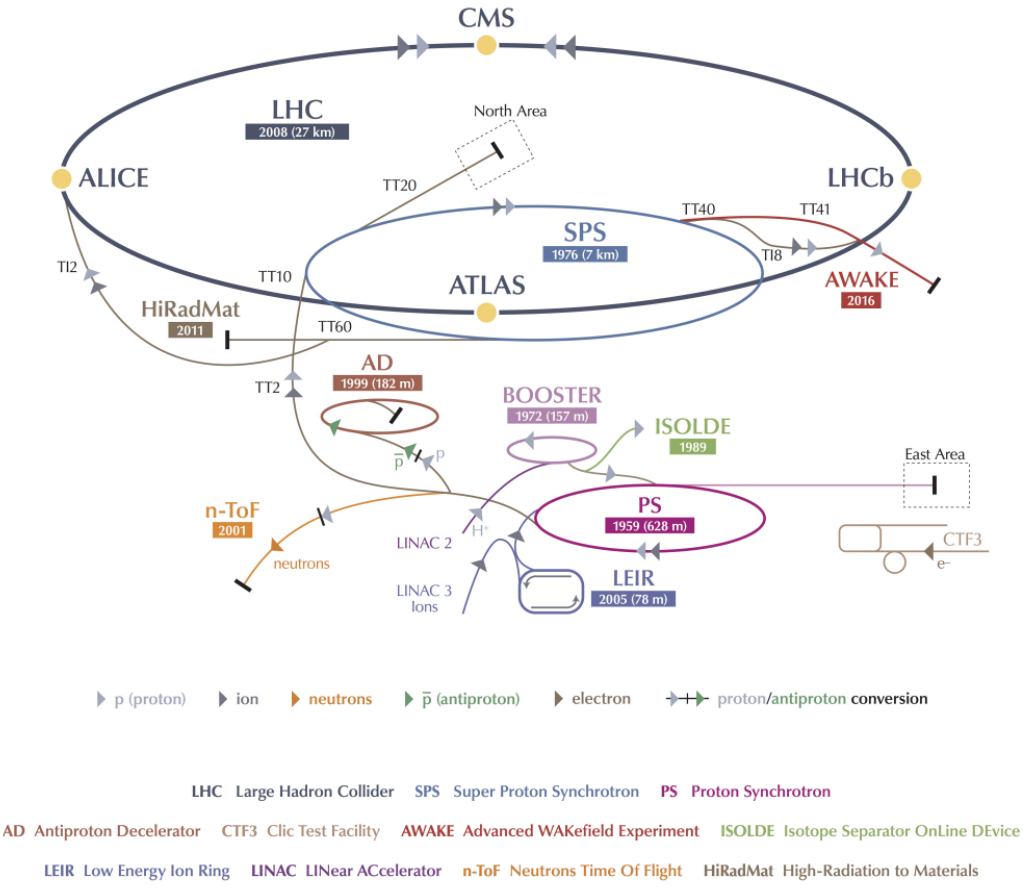

Figure 2.1: LHC injector complex [32]. The paths of all the different particles that can be accelerated are shown.

2.2 The LHCb experiment

LHCb is one of the four experiments installed on the LHC circumference [33, 34], and is dedicated to the study of hadrons containing beauty and charm

quarks. The detector is designed as a single-arm forward spectrometer, with a geometrical acceptance region of $[10, 250]$ mrad in the vertical plane and $[10, 300]$ mrad in the horizontal plane, corresponding to a pseudorapidity[1] acceptance region $1.6 < \eta < 4.9$; this choice is justified by the fact that $b\bar{b}$ and $c\bar{c}$ pairs generated from pp collisions are focused in the forward and backward direction with respect to the beam direction (Fig. 2.2).

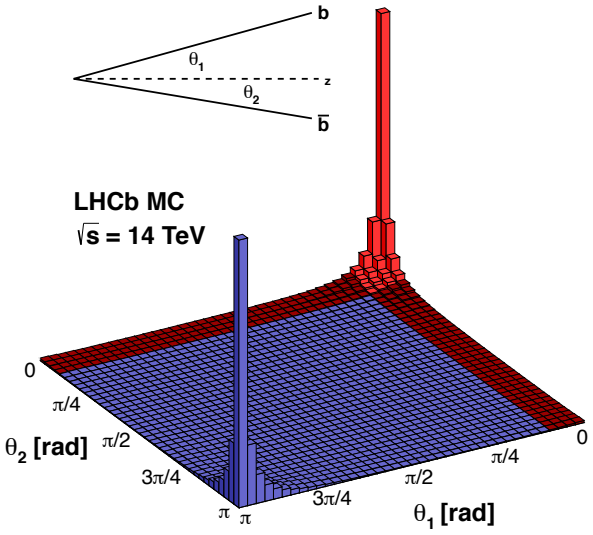

Figure 2.2: Simulated production angles of $b\bar{b}$ quark pairs at LHCb (the z axis corresponds to the beam direction).

In order to keep pile-up at a sustainable level and to reduce radiation damage of the components of the detector, the luminosity at the interaction point of LHCb is kept lower than the maximum luminosity achievable by LHC. This is done via a luminosity leveling technique: the proton beams start away from each other, and are progressively brought closer to one another as the beam intensity degrades, therefore maintaining the instantaneous luminosity approximately constant over time, up to $5 \times 10^{32}\,\mathrm{cm}^{-2}\,\mathrm{s}^{-1}$ in 2018. The integrated luminosity collected by LHCb during its operation life is shown in Fig. 2.3.

[1]The pseudorapidity of a particle travelling at a polar angle θ with respect to the beam axis is defined as

$$\eta = -\log\left(\tan\frac{\theta}{2}\right)$$

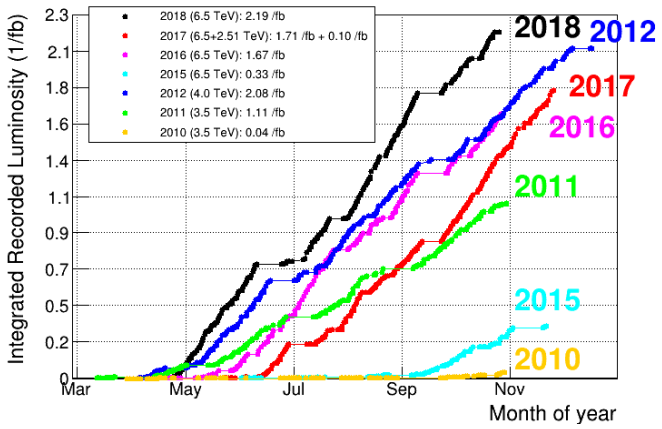

Figure 2.3: Integrated luminosity collected by LHCb every year from 2010 to 2018.

A cross-sectional lateral view of the LHCb detector is shown in Fig. 2.4. A right-handed coordinate system (x, y, z) is defined so that the z axis is parallel to the beam line and the y axis points vertically upwards. The apparatus contains many different sub-detectors with different scopes, that can be divided in two categories:

- The tracking system, consisting of the VErtex LOcator (VELO), the magnet, the Tracker Turicensis (TT), and three tracking stations (T1-T3);

- The particle identification system, that includes the two Ring Imaging CHerenkov detectors (RICH1 and RICH2), the electromagnetic calorimeter (SPD, PS, and ECAL), the hadronic calorimeter (HCAL), and the five muon stations (M1-M5).

In the following sections these sub-systems will be briefly described.

2.3 Tracking system

The tracking system is used to reconstruct the tracks of charged particles flying through the detector by joining the hits deposited in the tracking devices, and to measure their momentum thanks to the trajectory's curvature in a magnetic field.

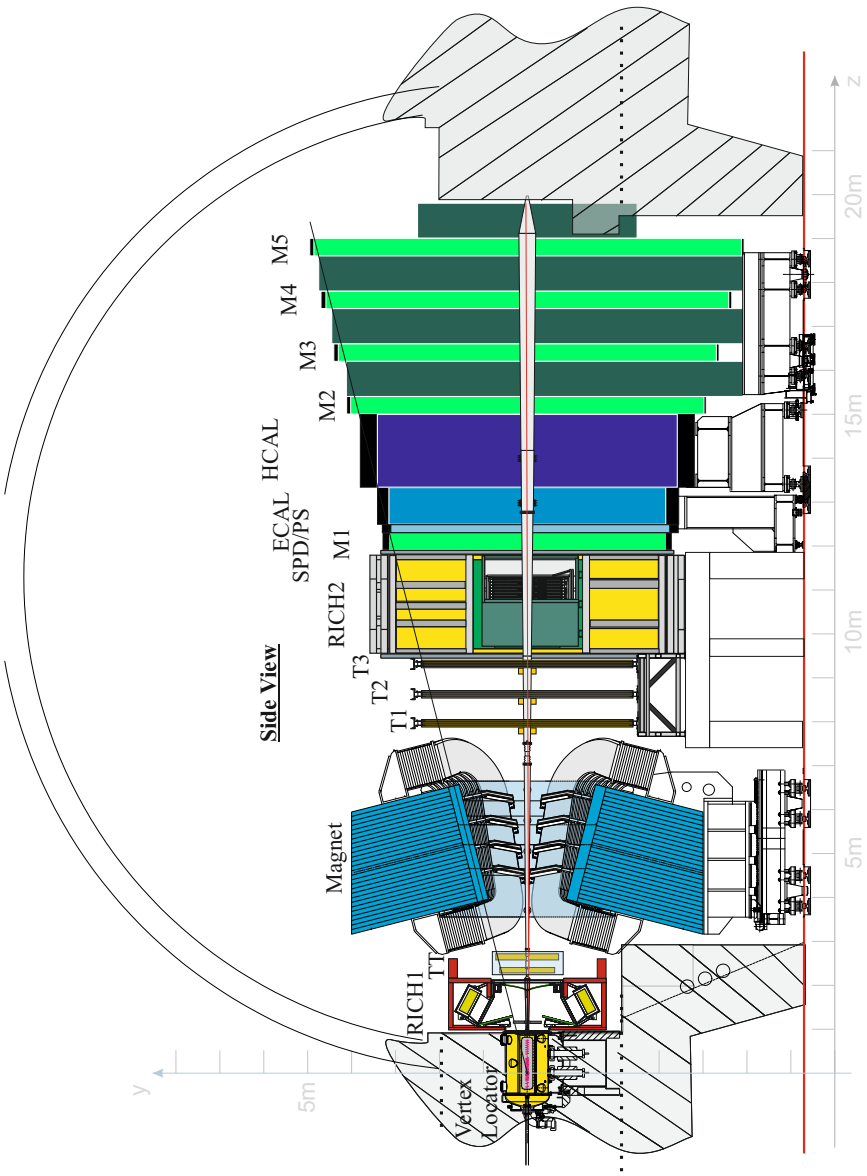

Figure 2.4: Lateral cross-section of the LHCb apparatus; the many sub-detector systems are indicated.

2.3.1 VELO

Beauty and charm hadrons can travel distances around 1 cm inside the detector before decaying. That means that a clear signature of such a particle being produced at LHCb is the presence of a secondary vertex close to the interaction point. To exploit this feature micro-metric precision of the position of the secondary vertex is crucial to efficiently select signal events while rejecting most of the background. A high spatial resolution also improves the measurement of the decay time of these particles, which is a key ingredient in time-dependent analyses.

The VELO sub-detector [35] is dedicated at reconstructing the position of the primary vertex (PV), identifying secondary vertices close to the interaction point, and detecting the tracks of the decay products of b- and c-hadrons.

The sub-detector is composed of 21 circular modules placed orthogonally to the beam line, each made of two overlapping halves of 300 µm thick radiation-tolerant silicon strip sensors. Two types of sensors are adopted in each module, which can measure either the radial distance or the azimuthal angle of the hit. Two additional modules, equipped with radial sensors only, are placed upstream of the interaction point, to provide pile-up information during the run. A schematic view of the VELO can be seen in Fig. 2.5.

The two halves of the sub-detector are initially placed at a safety distance of 3 cm from the beam during the proton injection of the LHC, to reduce radiation damage until the beams are stable, after which the sub-detector is brought to the closed position, with the module only 7 mm away from the beam tube.

The main performance figures of the VELO [36] are the following:

- PV position resolution: this improves with the number of reconstructed tracks in the sub-detector: as an example, with 25 tracks in the VELO the PV position is determined with a resolution of 13 µm in the x-y plane, and 71 µm in the z direction;

- Impact parameter (IP) resolution: the IP of a track is defined as the distance between the track and the PV; its resolution depends on the momentum of the particle, and it tends asymptotically to 12 µm for high-p_{T} particles;

- Decay-time resolution: the decay time of a particle of mass m and momentum p travelling for a distance l before decaying is computed as $t = ml/p$, so its resolution depends on the spatial resolution of the decay length; when tested on $B_s^0 \to J/\psi\,\phi$ decays, VELO allowed for a decay-time resolution of approximately 50 fs.

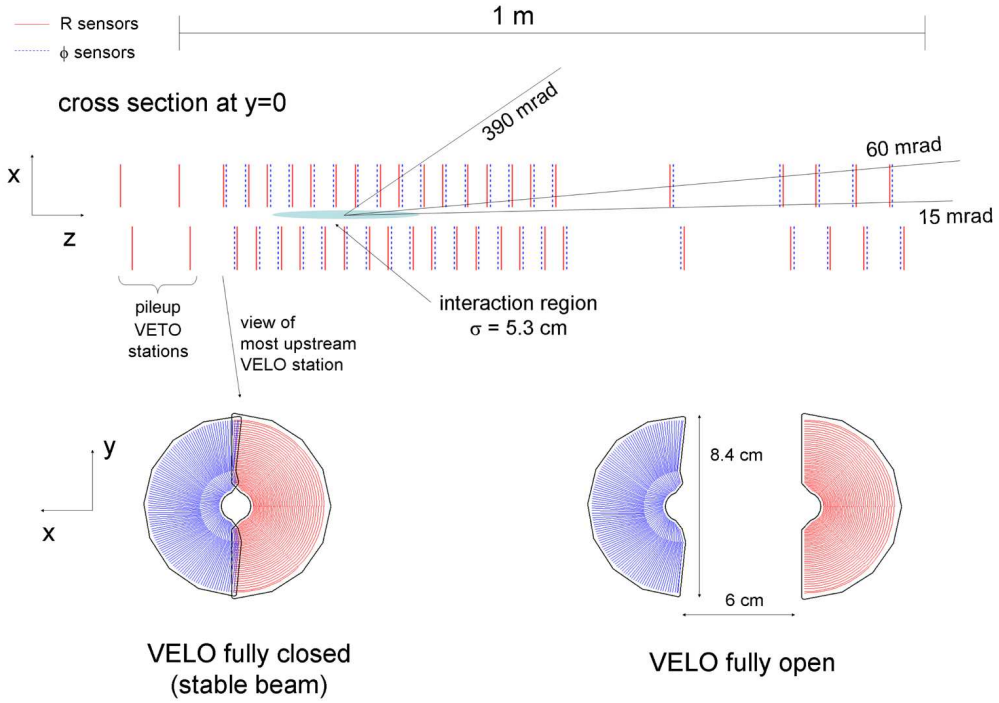

Figure 2.5: Cross-section of the VELO silicon sensors in the (x, z) plane, at $y = 0$. The front face of a silicon sensor is shown in both the fully closed and fully open positions.

2.3.2 Tracker Turicensis

The TT is positioned after RICH1 and before the dipole magnet, at a distance of 2.4 m from the interaction region; it is composed of two stations with dimensions $150 \times 130\,\mathrm{cm}^2$, called TTa and TTb, that cover the full LHCb acceptance region. Each station is divided in two layers made of 500 µm thick silicon micro-strips with a pitch of 183 µm. The first and fourth layer are oriented parallel to the vertical axis, while the second and third layer are rotated by $+5°$ and $-5°$, to provide information on both the x and y coordinate of the hits. This layout is shown in Fig. 2.6.

The single hit position resolution of the TT is about 52 µm. This sub-detector is designed to reconstruct the trajectories of low-momentum particles that are deflected out of the LHCb acceptance region by the magnet and long-lived particles that decay outside of the VELO region; it also helps combinining tracks from the VELO with those reconstructed in the downstream tracking stations, to improve momentum resolution and reduce the number of fake tracks.

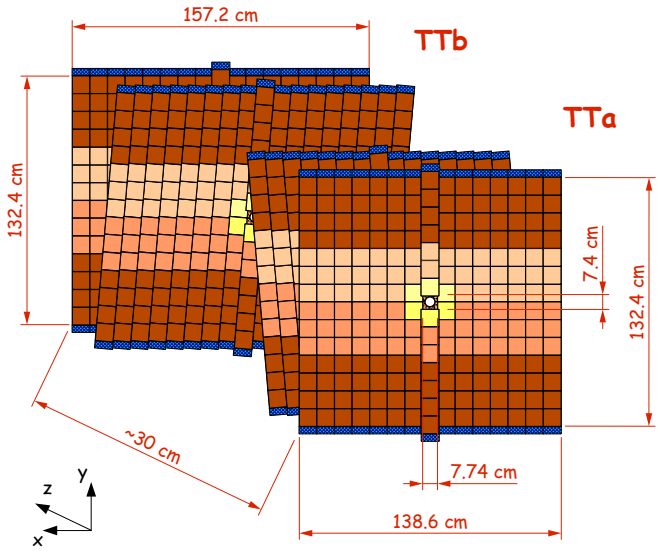

Figure 2.6: Layout of the four TT layers. Different colors distinguish between different readout sectors.

2.3.3 Tracking stations

Three tracking stations, T1, T2, and T3 are placed behind the magnet. Each station is divided in two section, based on the distance from the beam line: the Inner Tracker (IT) [37] and the Outer Tracker (OT) [38].

The IT surrounds the beam pipe with a surface of approximately 158×22 cm^2, with the use of four detector boxes arranged in a cross-shaped area. Each box contains four sensitive layers, arranged in the same ways as the TT. Every layer is made of seven modules of microstrip silicon sensors with a strip pitch of 200 µm (Fig. 2.7). This sub-detector has to sustain a larger particle flux near the beam pipe and tolerate a higher dose of radiation; this microstrip silicon technology is employed to ensure a better spatial resolution where most of the particles detected by LHCb will be reconstructed. The single hit position resolution of the IT is around 55 µm.

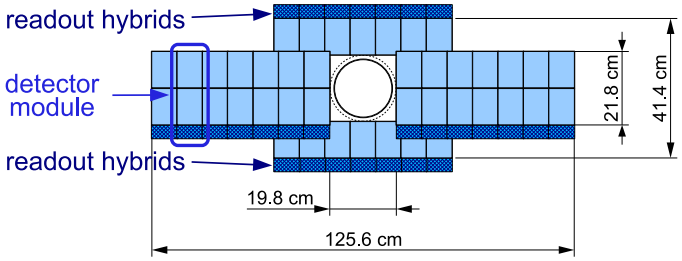

Figure 2.7: Layout and dimensions of the IT modules.

The OT fills the remaining part of the tracking stations, further away from the beam line, where the particle flux and occupancy is expected to be lower. This allows the use of a more cost-effective technology, *i.e.* straw tubes. The OT consists of three stations made of four individual modules, once again oriented in the same fashion as the TT. In each module, two staggered layers of straw tubes with a diameter of 4.9 mm are disposed as can be seen in Fig. 2.8. The tubes are filled with a mixture of Argon (70%), and CO_2 (30%), which translates to a drift time of around 35 ns and a single hit resolution of 205 µm.

2.3.4 Magnet

In a modern particle physics detector, the momentum of charged particles is inferred by measuring the curvature of their tracks in a magnetic field. For this reason, LHCb is equipped with a warm (*i.e.* non superconductive) dipole magnet, located between TT and the first tracking station T1.

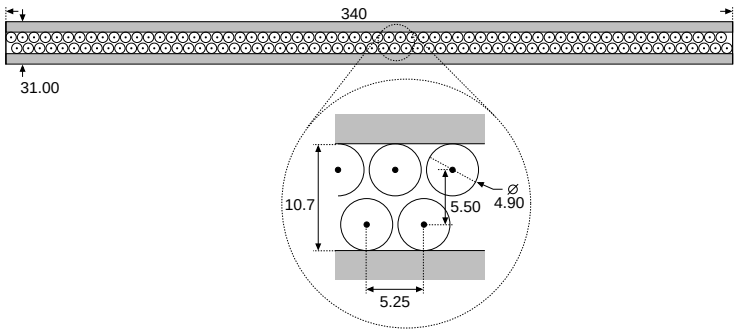

Figure 2.8: Illustration of an OT module, with the arrangement of the straw tubes inside.

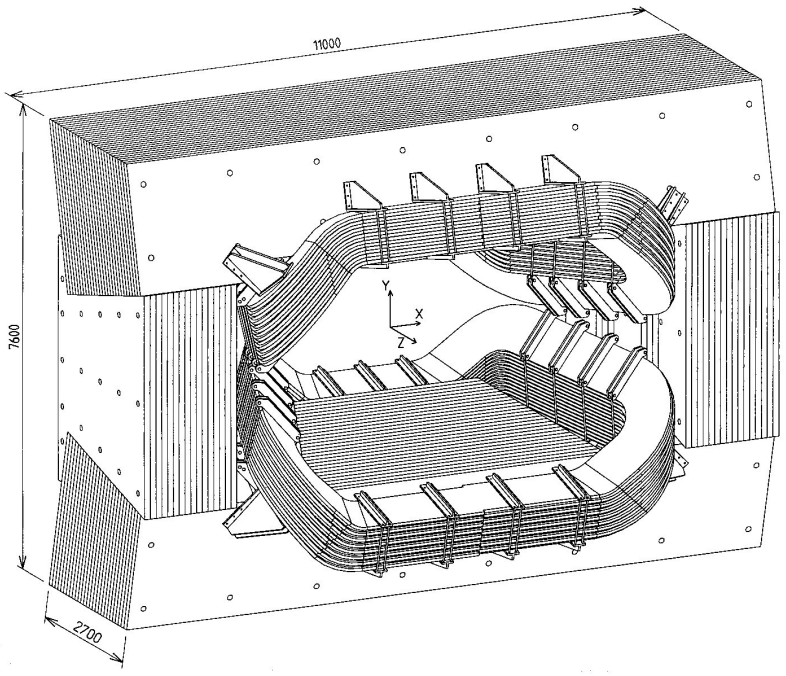

Figure 2.9: View of the LHCb dipole magnet.

The magnet [39] is composed of two trapezoidal aluminium coils weighting 54 tonnes, bent at 45° on the two transverse sides in a saddle shape (Fig. 2.9), placed inside an iron yoke with a total mass of around 1500 tonnes. The magnet coils are slightly inclined with respect to the z axis in order to follow the profile of the detector acceptance. The nominal current inside the coils is 5.8 kA, with a peak of 6.6 kA. The magnetic field is mainly directed in the y direction, as shown in Fig. 2.10, with a maximum field intensity of 1.1 T, and an integrated magnetic field of 3.7 T m.

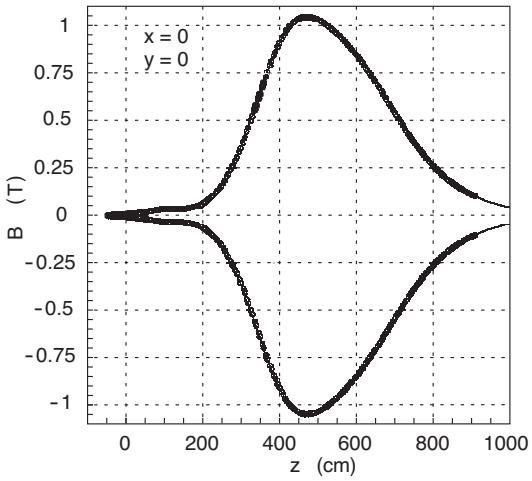

Figure 2.10: Intensity of the magnetic field component B_y along the z direction.

A relevant feature of LHCb's magnet is the possibility of switching its polarity during data-acquisition. This allows a precise control of charge effects inside the detector; since particles hit preferentially one side of the detector depending on their charge, reversing the magnet's polarity periodically yields a data sample where possible detection asymmetries are expected to cancel. To achieve this, during each Run the polarity of the magnet is reversed approximately every two weeks.

The momentum resolution $\delta(p)/p$ as a function of the particle's momentum p was measured with $J/\psi \to \mu^+\mu^-$ decays. As shown in Fig. 2.11, the momentum resolution is about 5 per mille for particles with a momentum below 20 GeV/c, and up to 8 per mille for a momentum of 100 GeV/c.

2.4 Particle identification system

Particle identification (PID) is a necessity for heavy flavour physics, since the decay products of b- and c-hadrons need to be precisely identified to allow a

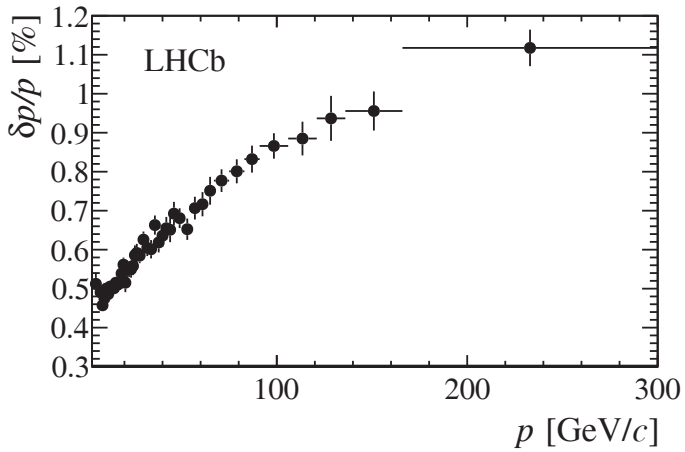

Figure 2.11: Relative momentum resolution versus momentum for tracks traversing the whole LHCb detector.

correct invariant mass reconstruction. At LHCb, this task is fulfilled by two RICH detectors, electromagnetic and hadronic calorimeters, and four muon stations. These systems will be described in the following sections.

2.4.1 Cherenkov detectors

Two Cherenkov detectors, RICH1 located directly after the VELO and RICH2 placed between T3 and the first muon station, are used to identify charged kaons, pions, and protons [40]. The structure of the two sub-detectors can be seen in Fig. 2.12; both devices are based on the detection of Cherenkov radiation, which is electromagnetic radiation emitted by a charged particle passing through a medium with a velocity higher than the speed of light in said medium. This radiation is emitted in the forward direction, producing a cone of light of aperture angle θ_C such that

$$\cos\theta_C = \frac{1}{\beta n}, \tag{2.1}$$

where β is the velocity of the particle in units of the speed of light in vacuum, and n is the refractive index of the medium. Cherenkov radiation is emitted as long as the particle's velocity is higher than the threshold value $\beta_{\text{thr}} = 1/n$. Therefore, by measuring the angle of emission of Cherenkov radiation a particle's velocity is obtained, and combining it with the momentum its mass can be inferred.

Two Cherenkov detectors, filled with different radiating mediums, are needed to discriminate particles at different momentum ranges. RICH1 uses

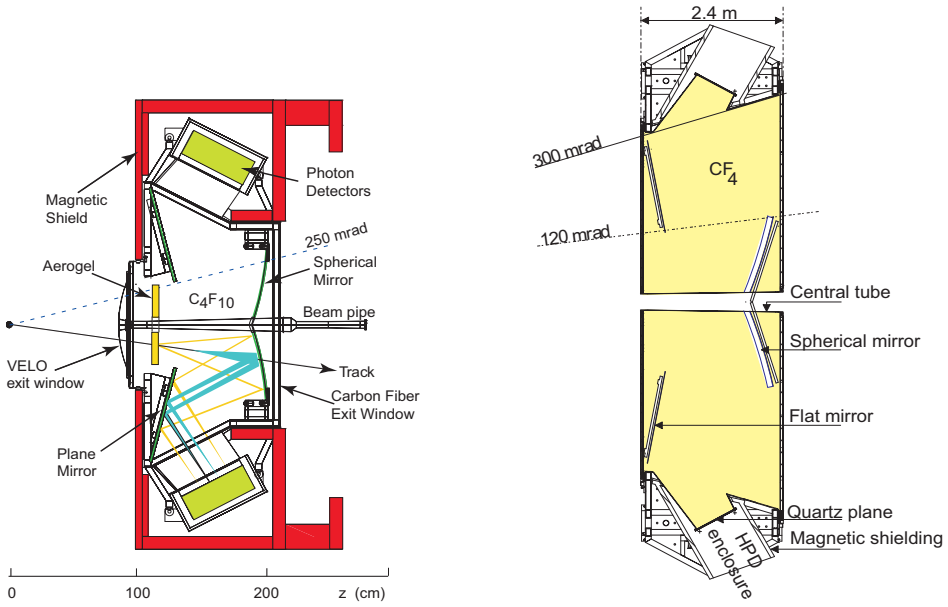

(a) RICH1 (b) RICH2

Figure 2.12: Side view of the two LHCb Cherenkov detectors.

silica aerogel ($n = 1.03$) and C_4F_{10} ($n = 1.0014$) to identify particles with momentum ranging from 1 GeV/c to 60 GeV/c within the acceptance region. During the first Long Shutdown (LS) between Run 1 and Run 2, the aerogel radiator was removed from RICH1 to extend the length of the gas radiator [41].

Particles flying in a straight line out of the interaction point pass through the radiator and emit Cherenkov radiation (provided the threshold condition is satisfied); photons are then reflected by two mirrors that focus light on a plane of Hybrid Photon Detectors (HPDs), sensitive to radiation wavelenghts in the range $200 - 600$ nm, which allow to measure the angle of emission of the radiation.

RICH2 contains a CF_4 gas radiator ($n = 1.0005$), capable of discriminating particles with momentum from 15 GeV/c up to more than 100 GeV/c. RICH2 has the same layout of RICH1, with two reflective mirrors and an array of HPDs for collecting Cherenkov photons. In both detectors the HPDs are placed in a metallic box to shield from the residual magnetic field, which could impact the HPDs efficiency.

In Fig. 2.13 is shown the distribution of the Cherenkov angle as a function of track momentum. It can be seen that different particles, having unique masses, populate specific regions of the plane, therefore allowing their discrimination.

For each track the likelihood that it is an electron, muon, pion, kaon,

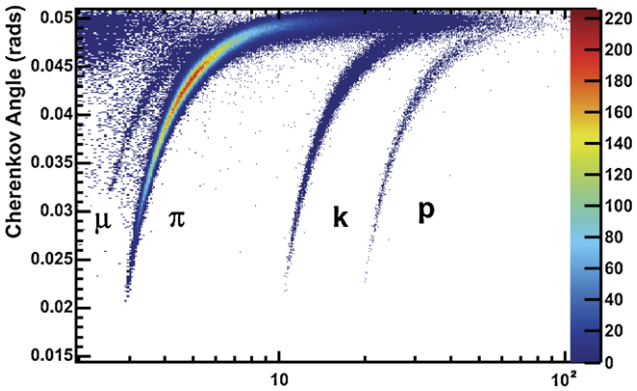

Figure 2.13: Reconstructed Cherenkov angle as a function of track momentum in the RICH1 C_4F_{10} radiator for different particles.

or proton is computed. A mass hypothesis is then assigned based on the difference between the log-likelihoods (often called DLL) for different particles; for example, a requirement of $\mathrm{DLL}_{K\pi} = \log\mathcal{L}(K) - \log\mathcal{L}(\pi) > 0$, when averaging over the momentum range $2 - 100\,\mathrm{GeV}/c$, gives a kaon selection efficiency of 95% and a pion misidentification fraction of 10%. A more stringent requirement, $\Delta\log\mathcal{L}(K-\pi) > 5$, reduces the pion misidentification rate to 3% with a kaon selection efficiency of 85%. The distribution of the two efficiencies as a function of track momentum can be seen in Fig. 2.14.

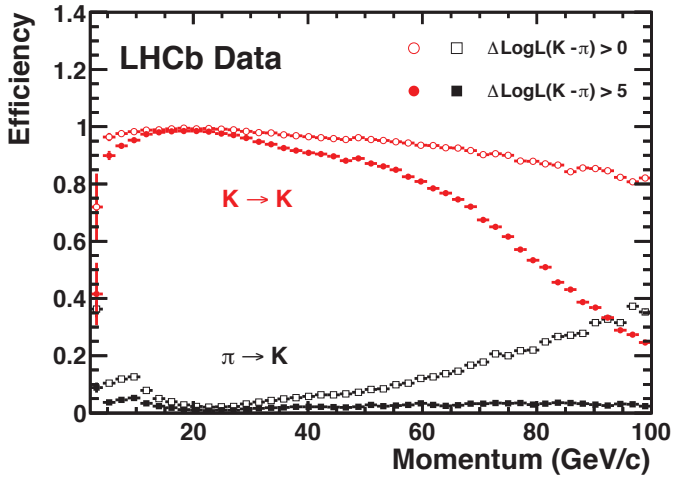

Figure 2.14: Kaon selection efficiency (red circles) and pion misidentification rate (black squares) as a function of track momentum for different PID requirements (filled and open markers).

2.4.2 Calorimeters

Calorimeters are used to measure the energy of the particles produced in the pp collisions, and they provide useful informations on the transverse energy (E_T) for the first trigger level (L0). They help in identifying electrons, photons and hadrons as well as in measuring their position.

The calorimeter system of LHCb [42] is composed of four devices, which from closest to furthest from the interaction point are: the Scintillating Pad Detector (SPD), the PreShower detector (PS), the electromagnetic calorimeter (ECAL), and the hadronic calorimeter (HCAL).

All four sub-detectors are sampling calorimeters, made of several layers of a scintillating material and an absorbing material. Particles traversing the active layers lose energy via electromagnetic or hadronic interactions, which excite the atoms of the scintillating material that emit ultraviolet radiation. Light is then carried away by wavelength-shifting (WLS) fibres to multi-anode photomultipliers (MAPMTs) located outside the detector, which count the collected photons. The total energy deposited in the calorimeter is proportional to the initial energy of the particle crossing it, therefore by measuring the former it is possible to estimate the latter.

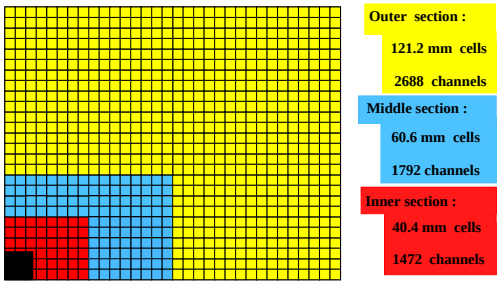

(a) ECAL, SPD, PS

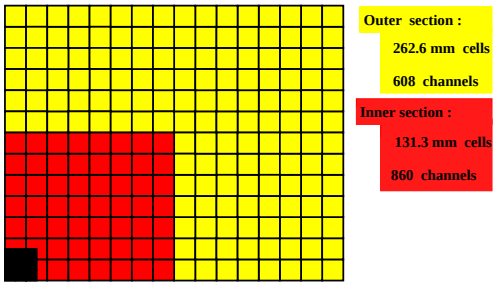

(b) HCAL

Figure 2.15: Lateral segmentation of one quadrant of the electromagnetic and hadronic calorimeters.

Since the hit density is expected to be higher in close proximity of the beam pipe, all calorimeters are divided in cells of variable lateral segmentation, three for SPD, PS, and ECAL, two for HCAL, as shown in Fig. 2.15.

The SPD/PS detector consists of a 15 mm (2.5 X_0) thick lead converter sandwiched between two planes of scintillating pads with a 15 mm thickness. The SPD performs the discrimination between charged particles and neutral, high-E_T particles such as π^0, while the PS is used to distinguish electrons from charged pions.

For a good energy resolution, full containment of the electromagnetic

shower is required; for this reason, the ECAL has a thickness of 25 X_0. Based on the shashlik technology, ECAL is made of 66 lead slices 2 mm thick, sandwiched between two 4 mm thick scintillator plates, with holes to accommodate the WLS plastic fibres. The energy resolution of the ECAL is

$$\frac{\sigma(E)}{E} = \frac{9.5\%}{\sqrt{E\,[\mathrm{GeV}]}} \oplus 1\%. \tag{2.2}$$

Since trigger requirements do not ask for a high energy resolution on hadronic particles, the HCAL does not need to fully contain the remaining showers. Therefore, the last calorimeter has a thickness of 1.2 m, corresponding to 5.6 hadronic interaction lengths (λ_{int}). The absorbing material consists of 16 mm iron plates, interspersed with 4 mm scintillator planes. This design results in an energy resolution of

$$\frac{\sigma(E)}{E} = \frac{(69 \pm 5)\%}{\sqrt{E\,[\mathrm{GeV}]}} \oplus (9 \pm 2)\%. \tag{2.3}$$

The energy resolution as a function of energy for both calorimeters can be seen in Fig. 2.16.

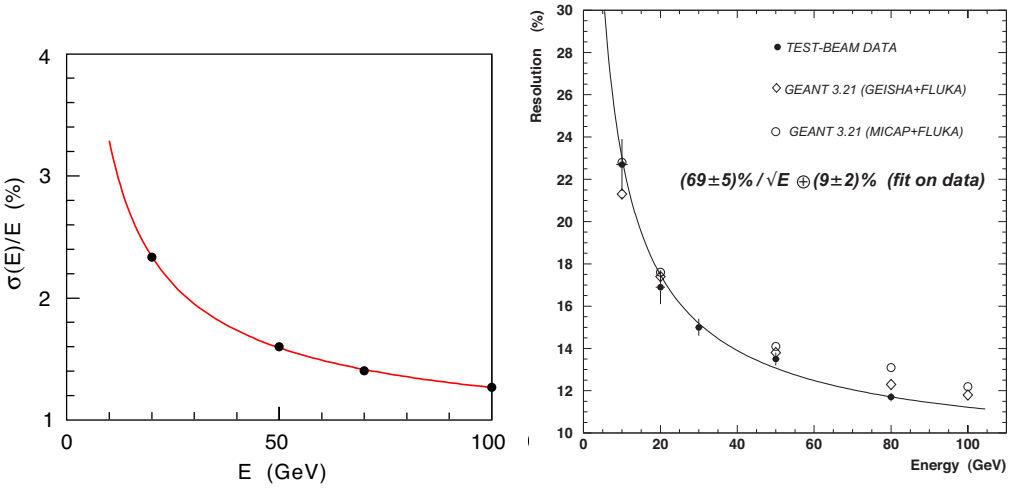

Figure 2.16: Energy resolution of the electromagnetic (left) and hadronic (right) calorimeters.

2.4.3 Muon stations

Muon triggering and offline identification is an essential requirement of the LHCb experiment, for the wide range of possible B decays containing muons in the final states, such as $B^0 \to J/\psi(\to \mu^+\mu^-)K^0_S$ and $B^0_s \to J/\psi(\to \mu^+\mu^-)\phi$.

The muon stations, the final step in the LHCb sub-detectors chain, are dedicated to the reconstruction of muons that traverse the whole detector without suffering major energy loss. The system is composed of five stations, the first of which (M1) is placed before the calorimeters, while the remaining four are located immediately after, each one separated by a 80 cm iron wall, as shown in Fig. 2.17. The absorbing material stops the surviving particles from the hadronic shower, allowing only the most penetrating leptons to pass through; only muons with momentum above 6 GeV/c reach the last stations M5.

Each station is divided in four concentric regions (called R1-R4, from closest to furthest from the beam axis) whose linear dimensions scale in the ratio 1:2:4:8 (Fig. 2.18), so that each region is expected to bear the same particle occupancy during data acquisition.

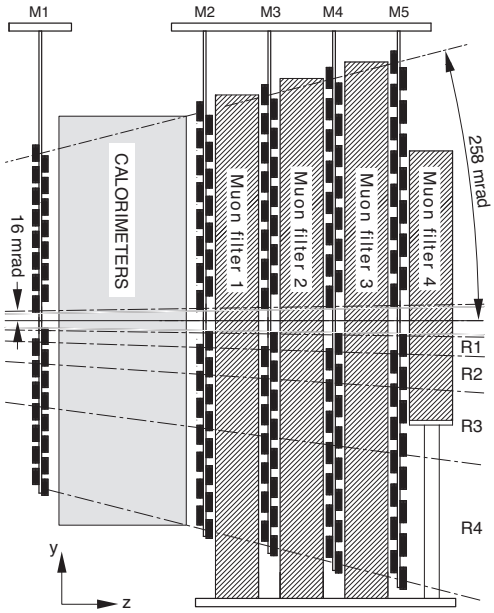

Figure 2.17: Layout of the five LHCb muon stations.

The sensitive layers of the muon stations are made of multiwire proportional chambers (MWPCs), except for region R1 of the first station, which is equipped with triple Gas Electron Multiplier (GEM) detectors, to better cope with the higher particle flux upstream of the calorimeters.

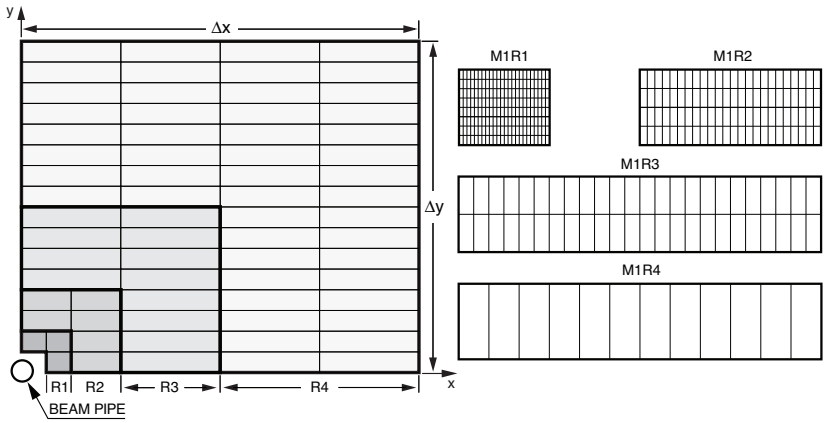

Figure 2.18: Front view of one quadrant of the muon station M1, where each rectangle identifies a region R1-R4 (left) and division of each region into logical pads (right).

2.5 Trigger

LHC collides protons at an astonishing rate of 40 MHz, although not all interactions that occur in the detector are interesting for physics analyses, hence most of the events need to be rejected, in order to save only the relevant ones with the limited bandwidth at which data can be written for storage.

The LHCb trigger [43] fulfills this purpose, by analyzing early signals in the detector to select the events more likely to include $b\bar{b}$ and $c\bar{c}$ pairs, reducing the output rate from 40 MHz to 2 kHz. This task is performed in three steps:

Level-0 (L0): the first level is a hardware implementation with custom electronics; its goal is to reduce the rate from 40 MHz to 1 MHz, at which point the full detector can be read out;

High Level Trigger 1 (HLT1): after digitization of all the event data, a software algorithm performs an inclusive event selection, reducing the output rate up to around 150 kHz;

High Level Trigger 2 (HLT2): in the last stage of the software trigger, an offline track reconstruction is performed with very loose cuts on particles' momentum and impact parameter; the surviving candidates are written to storage at a rate of 3.5 and 5 kHz in Run 1 and 12.5 kHz in Run 2.

A diagram of the LHCb trigger during different data-taking years is shown in Fig. 2.19. The three stages will now be described in greater details.

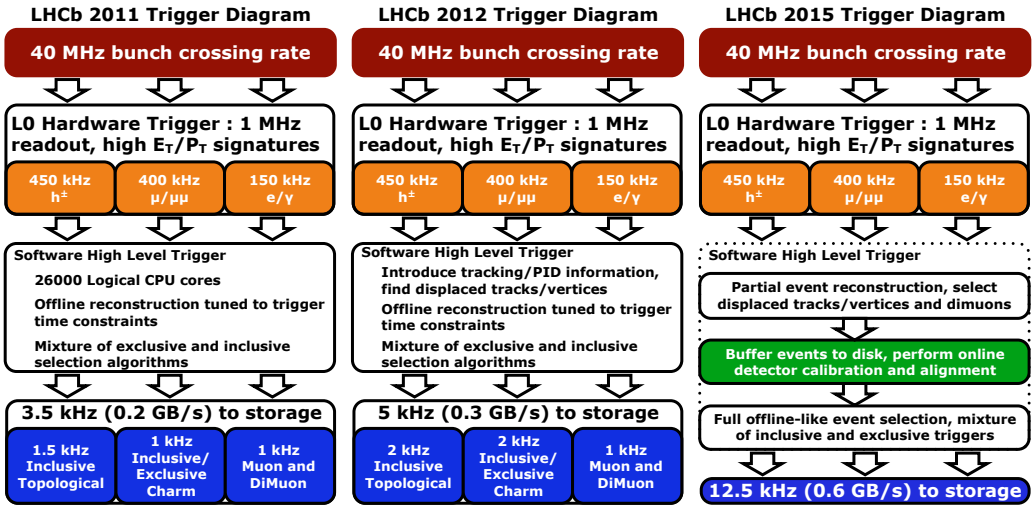

Figure 2.19: Trigger design during 2011 (left), 2012 (centre), and 2015 (right). During all Run 2 the trigger was set on the 2015 model.

2.5.1 Level-0

The Level-0 (L0) trigger exploits the most recognizable features of b- and c-decays, such as high-momentum and high-transverse energy (E_T) decay products, to distinguish physically relevant processes from minimum bias events. These signatures are searched as follows:

- A L0 calorimeter trigger looks for the largest deposit of transverse energy $E_T = \sum_i E_i \sin\theta_i$ in clusters of 2×2 cells in the calorimeters, while determining if the corresponding hits were produced by an electron (`L0Electron`), a photon (`L0Photon`), or a hadron (`L0Hadron`). The total number of hits in the SPD is also used to reject events with an excessive track multiplicity, which would exceed the timing capabilities of both the online and offline reconstruction algorithms;

- A muon trigger (`L0Muon`) searches for the two highest p_{T} tracks in the muon stations; fields of interest are defined around the recorded hits, the closest of which are joined in track segments and extrapolated to the nominal interaction point, giving an estimate of the transverse momentum.

The L0 trigger accepts an events if at least one of the above signature is detected which passes some defined threshold values for the E_T of hadrons ($\sim 3.7\,\mathrm{GeV}$) or electrons and photons ($3\,\mathrm{GeV}$), or for the p_{T} of the muons ($1.76\,\mathrm{GeV}/c$ for the highest-p_{T} muon or $1.6\,(\mathrm{GeV}/c)^2$ for the product of the

momentum of the two highest-p_{T} muons). The threshold values, especially for the p_{T} of the muon candidates, can be changed during the data acquisition period.

The information from the various L0 triggers are finally processed by a decision unit which takes the final decision to accept or reject the current event. The L0 decision must be made within 4 µs from the bunch crossing.

2.5.2 High Level Trigger 1

The High Level Trigger runs on an Event Filter Farm (EFF) containing up to 2000 computing nodes; a C++ application analyzes the entire detector data in parallel in each of the 29500 cores, although due to the 1 MHz L0 output rate and CPU limitations, most of the uninteresting events get rejected after evaluating only part of the available data. Being a software stage, this trigger is the more flexible, an can be quickly modified to implement a different strategy.

The first level, HLT1, uses the informations from the VELO to determine the PVs of the events and the IPs of the tracks, which are then passed to the next stage if they satisfy IP, momentum, and transverse momentum requirements, or if a muon was detected in the M stations.

Surviving events are passed through a Kalman Filter to perform a partial track reconstruction, and after a selection on the track and IP quality (χ^2 and χ^2_{IP}) they are passed to the last stage of the trigger.

2.5.3 High Level Trigger 2

The input rate of the HLT2 is sufficiently low to allow a full event reconstruction, almost identical to the one performed offline (the main difference being the lack of computation of the covariance matrix of the tracks parameters).

In this stage informations from the RICH detectors and calorimeters can also be used, so HLT2 is able to inclusively select b-hadron decays by means of topological requirements, such as the presence of a certain number of decay products correctly identified and displaced from the PV. Dedicated trigger lines can also be employed at this point to select specific final states for the various analyses.

Starting from Run 2 in the year 2015, LHCb has been using a new data stream called the Turbo stream [44] beside the traditional Full stream. The difference between the two streams is that while the Full stream saves all the information regarding the event that passed the trigger requests, the Turbo stream only saves the data relevant to the interesting decay, while discarding all the information from the rest of the event. This allows for data file sizes

smaller than the ones typically obtained with the Full stream, thus saving storage space. Offline reconstruction is usually not necessary, since the Turbo stream saves a sufficient amount of information; on the other hand, it is not possible to re-run the reconstruction of the full event at a later time due to the missing data from the rest of the event.

Starting from Run 3, the Turbo stream will become the standard way of processing and storing data from the LHCb detector.

Chapter 3

Measurement of y_{CP}

3.1 Introduction

In this Chapter, the procedure to measure the value of y_{CP} from $D^0 \to K^+K^-$, $D^0 \to \pi^+\pi^-$, and $D^0 \to K^-\pi^+$ decays is presented. The goal of this analysis is to update the previous LHCb measurement [30] with Run 2 pp collisions data collected by LHCb at a centre-of-mass energy $\sqrt{s} = 13\,\text{TeV}$, corresponding to an integrated luminosity of $5.57\,\text{fb}^{-1}$.

The analysis strategy can be summarised as follows:

- D^0 mesons coming from semileptonic B meson[1] decays are selected, and separated into samples according to the decay channel, $D^0 \to K^+K^-$, $D^0 \to \pi^+\pi^-$, $D^0 \to K^-\pi^+$;
- each sample is split into 18 exclusive D^0 decay-time bins;
- in each decay-time bin, a fit to the observed D^0 mass is performed to obtain the signal yield;
- the ratios of $D^0 \to h^+h^-$ and $D^0 \to K^-\pi^+$ signal yields as a function of decay time are computed,

$$R = \frac{\Gamma\left(D^0 \to h^+h^-, t\right)}{\Gamma\left(D^0 \to K^-\pi^+, t\right)} \frac{\varepsilon\left(D^0 \to h^+h^-, t\right)}{\varepsilon\left(D^0 \to K^-\pi^+, t\right)} \tag{3.1a}$$

$$\propto \frac{e^{-\hat{\Gamma}\left(D^0 \to h^+h^-\right)t}}{e^{-\hat{\Gamma}(D^0 \to K^-\pi^+)t}} \frac{\varepsilon\left(D^0 \to h^+h^-, t\right)}{\varepsilon\left(D^0 \to K^-\pi^+, t\right)} \tag{3.1b}$$

$$= e^{-\Delta_\Gamma^{hh} t} \frac{\varepsilon\left(D^0 \to h^+h^-, t\right)}{\varepsilon\left(D^0 \to K^-\pi^+, t\right)}, \tag{3.1c}$$

[1]The term "B meson" refers to both B^+ and B^0 mesons.

where h represents either a kaon or a pion, the effective decay widths $\hat{\Gamma}$ are defined in Eq. (1.48), $\varepsilon\,(D^0 \to f)$ is the decay-time acceptance, estimated from a Monte Carlo (MC) sample, and the parameter

$$\Delta_\Gamma^{hh} = \Gamma_{h^+h^-} - \Gamma_{K^-\pi^+}, \tag{3.2}$$

is the difference between $D^0 \to h^+h^-$ and $D^0 \to K^-\pi^+$ decay widths, obtained from a fit to the distribution of R;

- finally, y_{CP} is computed as $\Delta_\Gamma \tau_{D^0}$, where τ_{D^0} is the known experimental value of the average D^0 lifetime;
- systematic uncertainties are estimated from a number of possible sources.

Each stage of the analysis will be thoroughly explained in the following sections.

3.2 Data samples selection

The dataset used for the analysis were recorded by LHCb using dedicated Turbo trigger lines (see Sect. 2.5.3 for a brief description) across the years 2016, 2017, and 2018 (such lines were not implemented during the data-taking year 2015). Each signal candidate is obtained by reconstructing a D^0 meson and a muon that form a good vertex, compatible with a semileptonic decay of a B meson. The trigger requirements are:

L0 trigger: a muon from a signal candidate must fire the `L0Muon` trigger;

HLT1 trigger: a muon from a signal candidate must fire the line `Hlt1TrackMuon`, that requires a muon with high p_T and high χ^2_IP with respect to the primary vertex (PV)[2].

The reconstruction of the D^0 and B candidates is performed online by the HLT2 Turbo line, whose requirements are reported in Tab. 3.1. The reconstruction concerns the quality of the tracks[3] (P_track(Ghost) and χ^2_track/ndf), the kinematics (p and p_T), the topology (χ^2_IP), and particle identification ($\mathrm{DLL}_{K\pi}$). Candidate D^0 must satisfy some criteria on their invariant mass, the decay-vertex quality (χ^2_vertex/ndf), and the distance of the decay vertex to the PV (χ^2_VD). In the case of a B candidate, the selection uses requirements

[2] χ^2_IP is defined as the χ^2 difference between the vertex fit of a PV reconstructed with or without the particle in question.

[3] P_track(Ghost) is the ghost track probability, *i.e.* the probability for a track to be reconstructed from random combinations of hits in the detector.

Table 3.1: Selection requirements of the Turbo line for the $D^0 \to K^+K^-$, $D^0 \to \pi^+\pi^-$, and $D^0 \to K^-\pi^+$ decays.

Particle	Variable	Requirement
K, π from D^0	$P_{\text{track}}(\text{Ghost})$	<0.4
	p	$>2\,\text{GeV}/c$
	p_{T}	$>200\,\text{MeV}/c$
	χ^2_{IP}	>9
	$\text{DLL}_{K\pi}(K)$	>5
	$\text{DLL}_{K\pi}(\pi)$	<0
μ from B	$P_{\text{track}}(\text{Ghost})$	<0.4
	p	$>3\,\text{GeV}/c$
	p_{T}	$>1\,\text{GeV}/c$
	χ^2_{IP}	>9
	$\text{DLL}_{\mu\pi}(\pi)$	>0
D^0	$m(D^0)$	$\in [1775, 1955]\ \text{MeV}/c^2$
	$\chi^2_{\text{vertex}}/\text{ndf}$	<9
	χ^2_{VD}	>9
B	$m(B)$	$\in [2.3, 10.0]\ \text{GeV}/c^2$
	$m_{\text{corr}}(B)$	$\in [2.8, 8.5]\ \text{GeV}/c^2$
	$\chi^2_{\text{vertex}}/\text{ndf}$	<9
	$\cos(\text{DIRA})$	>0.999
	χ^2_{DOCA}	<10

on the visible and corrected invariant mass[4], the vertex reconstruction quality, the cosine of the angle between the momentum and the flight direction of the particle (DIRA), and the distance of closest approach (DOCA) between the decay products.

After the online selection, candidates are required to pass an offline selection which is summarised in Tab. 3.2. The requirements include: the χ^2/ndf of the DTF algorithm[5] applied to the D^0 and B decay chains; the distance between the D^0 and B decay vertices along the z direction, to suppress

[4]The corrected B mass is defined as $m_{\text{corr}}(B) = \sqrt{m(B)^2 + p_T(B)^2} + p_T(B)$, where $m(B)$ is the visible B invariant mass and $p_T(B)$ is the visible momentum component transverse to the B flight direction. This variable partially recovers the missing energy from the undetected neutrino or other invisible particles, thanks to momentum conservation.

[5]The DecayTreeFitter (DTF) algorithm consists of fitting a decay chain with multiple vertices with the help of a Kalman filter, allowing the extraction of decay time, position, and momentum parameters for all particles in the decay chain [45].

Table 3.2: Offline selection requirements for the decays $D^0 \to K^+K^-$, $D^0 \to \pi^+\pi^-$, and $D^0 \to K^-\pi^+$.

Variable	Requirement
DTF χ^2/ndf(B)	$\in [0, 9.5]$
DTF χ^2/ndf(D^0)	$\in [0, 6.5]$
$m(B)$	$\in [2500, 5000]$ MeV/c^2
$m_{\text{corr}}(B)$	$\in [4300, 5500]$ MeV/c^2
$p_\perp(D)$	$< 1.3 + 1.8 \times (m_{\text{corr}}\,[\text{GeV}/c^2] - 4.5)$ GeV/c $> 1.0 - 1.8 \times (m_{\text{corr}}\,[\text{GeV}/c^2] - 4.5)$ GeV/c
$z(D) - z(B)$	> 0 mm
$\text{DLL}_{K\pi}$ (K)	> 5
$\text{DLL}_{K\pi}$ (π)	< -5
J/ψ veto	$m(\mu^+\mu^-) \notin [3052, 3142]$ MeV/c^2 $m(\mu^+\mu^-) \notin [3631, 3741]$ MeV/c^2

combinatorial background when the D^0 vertex is reconstructed backwards with respect to the B candidate; the invariant mass and the corrected mass of the B candidate and the $\text{DLL}_{K\pi}$ of the D^0 decay products.

A J/ψ and $\psi(2S)$ veto is applied to avoid events where a muon originating from a $J/\psi \to \mu^+\mu^-$ decay is misidentified as a pion or kaon, by measuring the invariant mass between a muon and the opposite-charge decay product of the D^0. The candidate pairs with mass in a window of 45 MeV/c^2 around the J/ψ nominal mass and 55 MeV/c^2 around the $\psi(2S)$ nominal mass are discarded.

To suppress background events from unreconstructed decay products and semitauonic decay $B \to D^0\tau\nu X$, with $\tau \to \mu\nu\nu$, a requirement on the component of the D candidate momentum transverse to the B flight direction, $p_\perp(D)$, as a function of m_{corr} is applied.

After the cut-based selection, the remaining candidates are passed through a Boosted Decision Tree (BDT) classifier trained to distinguish between signal events and combinatorial background events where two independent pions or kaons have been randomly combined. In the training process, events in the $m(D^0)$ region $[1844, 1884]$ MeV/c^2 of the $D^0 \to K^-\pi^+$ decay are considered as purely signal events, while events lying in the sideband region $[1900, 1920]$ MeV/c^2 of the $D^0 \to K^+K^-$ decay are used as background. The BDT takes as input the transverse momenta of the two pions or kaons, the χ^2 of the B-vertex fit, the visible mass and the corrected mass of the B candidate.

The classifier assigns a numerical score to each event, ranging from -1 to 1 based on how likely the event is background or signal process, respectively.

The value is chosen as 0 in order to maximize the score function $S/\sqrt{S+B}$, where S and B are the expected number of signal and background events, respectively. This cut has a high background rejection of around 70% with a good signal efficiency, which is about 75%.

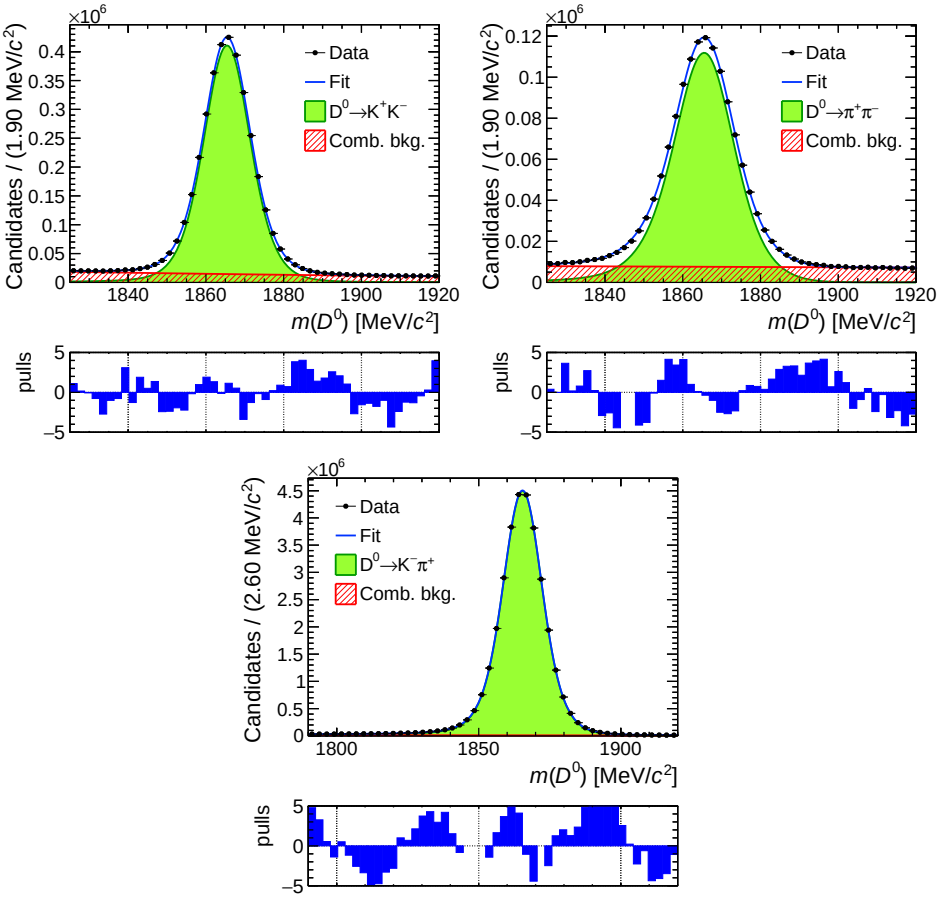

Figure 3.1: Fits to the time-integrated $m(D^0)$ samples in the $D^0 \to K^+K^-$ (top left), $D^0 \to \pi^+\pi^-$ (top right), and $D^0 \to K^-\pi^+$ (bottom) decay channel.

After the selection, a invariant mass fit as described in Sect. 3.3 is performed to the resulting invariant-mass distributions (Fig. 3.1) to extract the following signal yields

$$N(D^0 \to K^-\pi^+) = (32785.1 \pm 5.9) \times 10^3, \tag{3.3a}$$
$$N(D^0 \to K^+K^-) = (3452.4 \pm 2.1) \times 10^3, \tag{3.3b}$$
$$N(D^0 \to \pi^+\pi^-) = (1226.8 \pm 1.4) \times 10^3. \tag{3.3c}$$

A MC dataset is also used in the analysis to

1. gain a detailed overview of all sources of b-hadron decays that contribute to the sample;

2. model the relevant distributions used in the next steps of the analysis, in particular the decay-time acceptances and resolutions.

Simulated data undergo the same processing of reconstruction and selection as the experimental data. In Tab. 3.3, the amount of generated and selected events for the three decay channels are reported. When compared with Eq. (3.3), we can see that the number of selected-simulated events ranges from 1 to 3 times the number of selected-signal events in data, depending on the decay channel.

Table 3.3: Samples of simulated data used in the analysis; the second column reports the number of generated events; the last column reports the number of candidates after the full selection. Note that B indicates either a B^0 or a B^+.

Sample	Generated [10^6]	Selected [10^6]
$B \to D^0\mu\nu X$, $D^0 \to K^-\pi^+$	59.4	34.2
$B \to D^0\mu\nu X$, $D^0 \to K^+K^-$	14.7	8.3
$B \to D^0\mu\nu X$, $D^0 \to \pi^+\pi^-$	7.1	4.1

3.3 Decay-time bin analysis

The three decay channel samples are divided into 18 exclusive decay-time bins, with edges (in ps): 0.15, 0.20, 0.24, 0.30, 0.35, 0.41, 0.47, 0.54, 0.60, 0.68, 0.76, 0.84, 0.94, 1.04, 1.16, 1.29, 1.44, 1.63, 1.95. The binning scheme is optimised to contain approximately the same number of B candidates, as was done in Ref. [46]. Events over 1.95 ps are discarded due to the possible presence of different sources of background at high lifetime. Due to the low statistical power of those events, the final result will be not affected. Further studies, beyond the aim of this thesis, will be necessary to understand the origin of these background sources and include the events in the analysis before the final publication.

The D^0 decay time is computed from the data as:

$$t_{D^0} = \frac{m_{D^0}\vec{L} \cdot \vec{p}(D^0)}{p^2(D^0)}, \tag{3.4}$$

where $m_{D^0} = (1864.83 \pm 0.05)\,\text{MeV}/c^2$ is the known value of the D^0 meson mass [17], $\vec{L}$ is the vector connecting the B and D^0 decay vertices and $\vec{p}(D^0)$ is the reconstructed momentum of the D^0 candidate.

In each decay-time bin a binned maximum likelihood fit is performed to extract the signal yields; the function used to model the data is

$$\frac{N_{\text{sig}}}{N_{\text{sig}} + N_{\text{bkg}}} \left[\sum_{i=1}^{n} c_i \prod_{j=1}^{i-1} (1 - c_j) \mathcal{G}_i(x|\, \mu_i, \sigma_i, s) \right] + \frac{N_{\text{bkg}}}{N_{\text{sig}} + N_{\text{bkg}}} e^{\lambda x}, \tag{3.5}$$

where

$$\mathcal{G}(x|\, \mu, \sigma, s) = \int \Theta(\mu - x')(\mu - x')^s e^{-\frac{(x'-x)^2}{2\sigma^2}}\, \mathrm{d}x' \tag{3.6}$$

is the signal shape function, consisting of the convolution between a Gaussian function, a power law, and the Heaviside function Θ. This signal shape was derived from a calculation of the invariant mass spectrum of soft-photon QED radiation emitted by charged final state particles. The integration is performed over the entire mass range, which consist of the range $[1825, 1920]$ MeV/c^2 for the $D^0 \to K^+K^-$ and $D^0 \to \pi^+\pi^-$ decays and $[1790, 1920]$ MeV/c^2 for the $D^0 \to K^-\pi^+$ decay. N_{sig} and N_{bkg} are the signal and background event yields and also act as normalisation constants, and the c_i are the relative fractions of the signal components.

The number n represents the number of components used to estimate the signal yields, and is equal to 4 for the KK and $K\pi$ channel, and to 3 for the $\pi\pi$ channel; all components share the same tail parameter s, while they have independent peak and width parameters μ_i and σ_i; the last fraction c_n is equal to 1 to ensure that the signal probability density function is normalised correctly. An exponential distribution with coefficient λ is chosen to describe combinatorial background.

The signal shape parameters are estimated by a fit to the MC distributions, which contain only signal events. The values of these parameters are then fixed in the fits to the time-integrated and decay-time binned data samples, except for the mean and sigma of the first component μ_1 and σ_1, which are left floating. The shape parameters of the other components are written as $\mu_i = \mu_1 + \delta_i$ and $\sigma_i = k_i\sigma_1$, with δ_i and k_i fixed from the MC fits, to ensure that the signal shape is tied to the parameters of the first component. The other floating parameters are the normalisation constants N_{sig} and N_{bkg} and the background parameter λ. The results of the mass fits are presented in Appendix A.

3.4 Relative acceptance correction

Decay-time acceptance ratios need to be estimated from simulated events for two reasons:

1. the trigger algorithms use requirements on kinematic variables that modify the decay-time distribution of the D^0 meson candidates; therefore it is necessary to apply the same selection to MC samples to measure the selection efficiency as a function of decay time;

2. offline selection requirements have a different time-dependent efficiency on the three decay channels; by applying an acceptance correction to the signal yield ratios, these effects are taken into account.

The similarities between the $D^0 \to K^+K^-$, $D^0 \to \pi^+\pi^-$, and $D^0 \to K^-\pi^+$ decays result in close decay-time acceptances. These are determined from the simulated samples and are shown in Fig. 3.2. The variation of the acceptance ratio is within around 2% over the decay-time range considered. In the determination of Δ_Γ, the ratio of $h^+h^-/K^-\pi^+$ signal yields is divided by the acceptance ratio (see Eq. (3.1)), and the respective uncertainties are propagated accordingly.

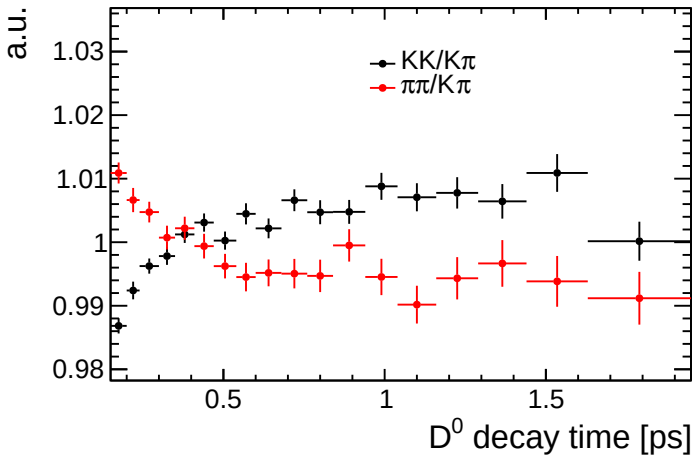

Figure 3.2: Ratios of decay-time acceptance $KK/K\pi$ (black) and $\pi\pi/K\pi$ (red).

3.5 Determination of Δ_Γ

The difference between the decay widths of $D^0 \to K^+K^-$ or $D^0 \to \pi^+\pi^-$ and $D^0 \to K^-\pi^+$ decays, Δ_Γ, is measured through a fit to the ratio of D^0 decay-time signal yields. Once the signal yields and their uncertainties are measured in each decay-time bin, a binned χ^2 fit is performed, which minimises the function

$$\chi^2 = \sum_{i=1}^{18} \frac{(n_i - R_i d_i)^2}{\sigma_{n_i}^2 + R_i^2 \sigma_{d_i}^2}, \tag{3.7}$$

where n_i and d_i are the numerator (KK or $\pi\pi$) and denominator ($K\pi$) signal yield in bin i, respectively, while σ_{n_i} and σ_{d_i} are their uncertainties. R_i is the expected ratio, defined as

$$R_i = N A_i \frac{\int_{T_i} \mathrm{pdf}_n(t_D)\,\mathrm{d}t}{\int_{T_i} \mathrm{pdf}_d(t_D)\,\mathrm{d}t}. \tag{3.8}$$

In the numerator the decays $D^0 \to K^+K^-$ or $D^0 \to \pi^+\pi^-$ decays are considered, in the denominator only $D^0 \to K^-\pi^+$ decays. T_i is the corresponding decay-time interval in bin i, A_i is the decay-time acceptance ratio between numerator and denominator as described in Sect. 3.4, and N is a normalisation factor.

The numerator and denominator pdfs are written as

$$\mathrm{pdf}_j(t_D) = e^{-\Gamma_j t_D}, \qquad (j = n, d) \tag{3.9}$$

where Γ_j is the decay width. In the denominator, $\Gamma_d = 1/\tau_{D^0}$ is fixed to the average D^0 decay width, with $\tau_{D^0} = 0.4101\,\mathrm{ps}$ [17]; in the numerator, the width is written as $\Gamma_n = \Gamma_d + \Delta_\Gamma$, with Δ_Γ determined by the fit. Therefore, the only free parameters in the fit are Δ_Γ and N.

3.6 Results

The acceptance-corrected fits to the signal yield ratio in bins of D^0 decay time are shown in Fig. 3.3; the numerical results are reported in Tab. 3.4, where the central values of Δ_Γ and y_{CP} are blind, *i.e.* shifted by an unknown random value. The same shift is used for both the KK and $\pi\pi$ sample. The blinding procedure is commonly adopted in the LHCb experiment to avoid bias on the final results induced by the analysts. The unblinding of the final result is done only once the internal review is completed. From the fitted value of Δ_Γ, y_{CP} is computed using the world average of the D^0 meson lifetime as input, $\tau_{D^0} = (0.4101 \pm 0.0015)\,\mathrm{ps}$ [17].

The measured values of y_{CP}^{KK} and $y_{CP}^{\pi\pi}$ are compatible to each other within 1.8 standard deviations. The analysis was also performed with the data samples separated by year of data acquisition (2016, 2017, and 2018), and the agreement between the measured values of y_{CP} in the various subsamples is summarised in the following matrix, whose entries are defined as $(y_{CP}^{i} - y_{CP}^{j})/\sqrt{\sigma(y_{CP}^{i})^2 + \sigma(y_{CP}^{j})^2}$:

$$\begin{array}{c} \\ KK16 \\ KK17 \\ KK18 \\ \pi\pi16 \\ \pi\pi17 \\ \pi\pi18 \end{array} \begin{array}{c} \begin{array}{cccccc} KK16 & KK17 & KK18 & \pi\pi16 & \pi\pi17 & \pi\pi18 \end{array} \\ \begin{pmatrix} 0 & -0.37 & 1.13 & 0.16 & -0.16 & -2.45 \\ & 0 & 1.53 & 0.42 & 0.10 & -2.20 \\ & & 0 & -0.59 & -0.96 & -3.35 \\ & & & 0 & -0.27 & -2.06 \\ & & & & 0 & -1.84 \\ & & & & & 0 \end{pmatrix} \end{array} \tag{3.10}$$

Since the matrix is antisymmetric by definition, the entries below the diagonal are omitted. The tension between the two decay channels in the 2018 data is evident. After several investigations, the origin has not been found yet. Recently the LHCb Collaboration has identified a bug in central code on the calculation of impact parameter error which is different between data and Monte Carlo and could bias the MC time-dependent efficiencies. Due to the non negligible time necessary to produce a new Monte Carlo data sample, it was not possible to further investigate this issue. However, when the results are averaged among the various data-taking years, the discrepancy is reduced to 1.8 standard deviations, pointing at a good compatibility between the results.

It is to be noted that the value of Δ_Γ is very weakly sensitive to the input value of the D^0 lifetime, which is fixed in Eq. (3.9). This is tested by varying τ_{D^0} by plus or minus 5 standard deviations. The corresponding value of Δ_Γ changes only by 2×10^{-5} at most, meaning that the uncertainty on the D^0 lifetime has no impact on the determination of Δ_Γ.

Another notable feature is that the ratio between the normalisation constants $N_{KK}/N_{\pi\pi} = 2.827 \pm 0.008$ is consistent with the ratio of the known values of the branching ratios of $D^0 \to K^+K^-$ and $D^0 \to \pi^+\pi^-$ decays 2.80 ± 0.06 [17], which can be expected for a selection efficiency very similar for the two samples.

3.7 Systematic uncertainties

Several sources of systematic uncertainties can contribute to bias the final results, namely the one associated with the assumed decay model and com-

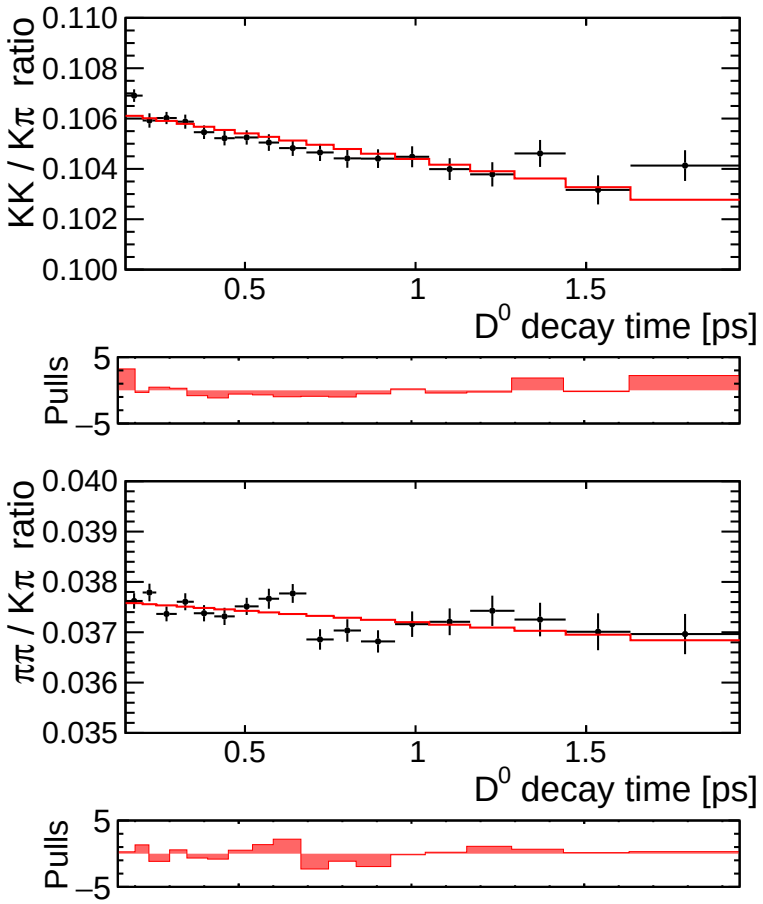

Figure 3.3: Plots of the acceptance-corrected signal yield ratios $KK/K\pi$ (top) and $\pi\pi/K\pi$ (bottom) in bins of D^0 decay time, with fit projection overlaid

Table 3.4: Results of the fit to extract $\Delta\Gamma$ and N. The χ^2/ndf of the fit, the correlation coefficient between the two parameters, and the corresponding value of y_{CP} are also reported. The central values of $\Delta\Gamma$ and y_{CP} are blind (see text).

	$KK/K\pi$	$\pi\pi/K\pi$
$\Delta\Gamma$ [ps^{-1}]	-1.8527 ± 0.0021	-1.8603 ± 0.0036
N	0.10648 ± 0.00015	0.03766 ± 0.00009
χ^2/ndf	25.4/16	23.7/16
$\rho(N, \Delta\Gamma)$	0.82	0.83
y_{CP} [%]	75.98 ± 0.09	76.29 ± 0.15

Table 3.5: Summary of the systematic and statistical uncertainties on Δ_Γ and y_{CP}.

	$\sigma(\Delta_\Gamma^{KK})$ [ps^{-1}]	$\sigma(\Delta_\Gamma^{\pi\pi})$ [ps^{-1}]	$\sigma(y_{CP}^{KK})$ [%]	$\sigma(y_{CP}^{\pi\pi})$ [%]
Simulated sample size	0.0011	0.0014	0.06	0.05
Total systematic	0.0011	0.0014	0.06	0.05
Statistical only	0.0018	0.0033	0.07	0.14

position of the simulated samples of semileptonic B decays; possible biases introduced by the fit method; the presence of irreducible background; the neglected decay-time resolution; and the limited size of Monte Carlo data samples. Preliminary studies on one of them have been carried out. Besides, an investigation on the possible presence of irreducible sources of background is started and will be concluded after the delivering of the thesis. The summary of the results obtained are reported in Tab. 3.5.

3.7.1 Simulated sample size

The statistical uncertainty on the limited size of the simulated MC sample used to compute the decay-time acceptances is propagated in the fit to extract Δ_Γ, and thus on the value of y_{CP} as well, so the results in Tab. 3.4 already include this contribution.

To disentangle this source of systematic uncertainty to the statistical error of the data, the fit is repeated without considering the uncertainty of the decay-time acceptance ratio histograms. The central value of Δ_Γ changes only by 1×10^{-5} and $5 \times 10^{-5}\,\text{ps}^{-1}$ for the channel $D^0 \to K^+K^-$ and $D^0 \to \pi^+\pi^-$, respectively, while the uncertainties get reduced to 0.0018 and $0.0033\,\text{ps}^{-1}$; these values are taken as the purely statistical uncertainties of Δ_Γ^{KK} and $\Delta_\Gamma^{\pi\pi}$.

The systematic uncertainty due to the limited simulated sample size is estimated as the difference in quadrature between the uncertainties of Δ_Γ from the baseline fit and the ones obtained by excluding the uncertainty of the acceptance ratio. This results in a systematic error of 0.0011 and $0.0014\,\text{ps}^{-1}$ for Δ_Γ^{KK} and $\Delta_\Gamma^{\pi\pi}$ and of 0.06 and 0.05 % for y_{CP}^{KK} and $y_{CP}^{\pi\pi}$, respectively; the purely statistical uncertainties are 0.07 and 0.14 % for y_{CP}^{KK} and $y_{CP}^{\pi\pi}$, respectively.

3.7.2 Additional background sources

An additional source of systematic error is the presence of background sources not effectively suppressed by the current selection, namely semileptonic decays with a similar topology as the signal processes. A way to study this source of background process is by use of the so-called wrong-sign (WS) $D^0 \to K^-\pi^+$ decays, as opposed to the right-sign (RS) decays. The two processes can be described as follows:

- RS events are the ones that come from Cabibbo-favoured (CF) signal events, which are $B \to D^0(\to K^-\pi^+)\mu^-\overline{\nu}X$ and $B \to \overline{D^0}(\to K^+\pi^-)\mu^+\nu X$, where the charge of the muon infers the flavour of the D^0 meson;

- WS events are the ones in which the D^0 meson decays into the *CP*-conjugate channel, that is $B \to D^0(\to K^+\pi^-)\mu^-\overline{\nu}X$ and $B \to \overline{D^0}(\to K^-\pi^+)\mu^+\nu X$; these decays are doubly-Cabibbo-suppressed (DCS), and thus about a factor of 10^3 less likely to occur than CF decays. When this happens, the flavour of the D^0 meson, initially assigned based on the charge of the muon, is switched to restore the CF decay signature, obtaining $B \to D^0(\to K^-\pi^+)\mu^+\overline{\nu}X$ and $B \to \overline{D^0}(\to K^+\pi^-)\mu^-\nu X$. Therefore, the right- and wrong-sign samples identify respectively a correct and an incorrect charge combination of the D^0 meson and the muon.

To verify the hypothesis that WS events accurately mimic the background, it must be verified that their kinematics is similar to that of background events in the RS sample: in order to do this, the distributions of several kinematic variables from the RS and WS samples were compared in the background region $m(B) > 5500\,\text{MeV}/c^2$.

The variables chosen to be studied are the visible B mass (on the whole mass spectrum), the visible D^0 mass, the D^0 decay time, the muon momentum and transverse momentum, and the muon PID. The plots of these distributions are shown in Fig. 3.4.

Comparing the RS and WS distributions of the selected variables in the background region, it can be seen that they share many similarities, especially regarding the invariant D^0 mass, the D^0 decay time and the visible B mass in the background sideband.

Taking these observations into consideration suggests that WS events can be considered as a suitable proxy for the background, and therefore can be used to study the decay-time distribution of the latter. The next step is to compute the WS event yields in the data and then extrapolate this yield in

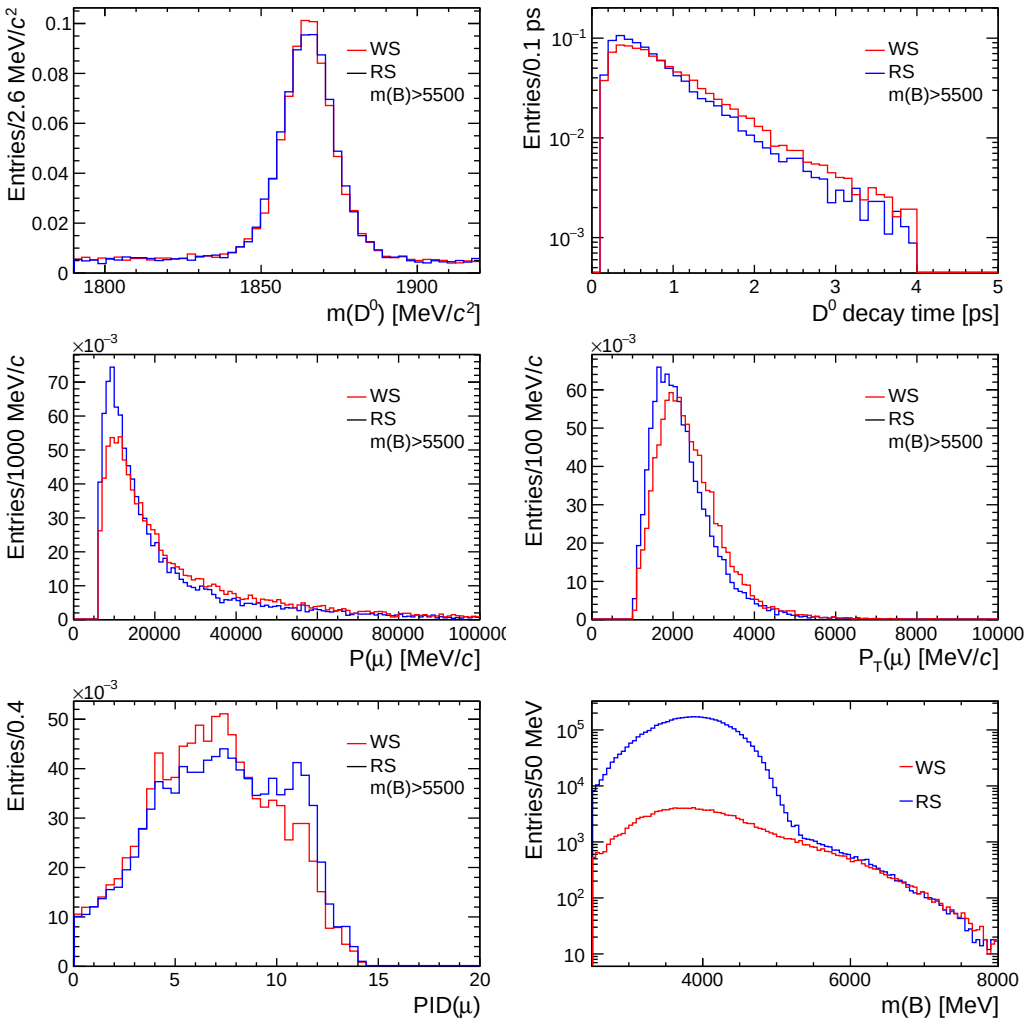

Figure 3.4: Distributions of the kinematic variables for the RS and WS data samples. It is shown the D^0 invariant mass (top left), the D^0 decay-time (top right, log scale), the muon momentum (middle left) and transverse momentum (middle right), the muon PID score (bottom left), and the visible B mass (bottom right, log scale). All distributions are normalised, except the visible B mass.

the signal region for an estimation of this source of background, $N_{\rm bkg}(h^-h^+)$ and $N_{\rm bkg}(K^-\pi^+)$.

In the case of $D^0 \to K^-\pi^+$ decays, the estimate can be done directly on the WS data sample,

$$N_{\rm bkg}(K^-\pi^+) = \Sigma_{K\pi} \cdot {\rm WS}(K^-\pi^+), \tag{3.11}$$

where $\Sigma_{K\pi}$ is a scale factor depending on the result of the extrapolation of sideband events in the signal region, calculated using simulated events, and ${\rm WS}(K^-\pi^+)$ are the number of WS events in the sideband. In the cases of $D^0 \to K^+K^-$ and $D^0 \to \pi^+\pi^-$ decays, it is assumed that the WS data sample is still a good proxy for the background estimation and the number of background events are calculated as

$$N_{\rm bkg}(h^+h^-) = \Sigma_{hh} \cdot {\rm WS}(K^-\pi^+), \tag{3.12}$$

where Σ_{hh} is the scale factor calculated using $D^0 \to h^+h^-$ MC events.

Once the background yields are determined, they can be subtracted to the signal yields in order to evaluate the impact of this source of systematic uncertainty on the final measurement.

The main part of the analysis to measure the value of y_{CP} is already set up. The evaluation of other sources of systematic errors and cross-checks are still necessary before the publication on a peer-reviewed journal and need additional studies that are beyond the aim of this thesis.

3.8 Final result

The charm-mixing parameter y_{CP} was measured using $D^0 \to K^+K^-$, $D^0 \to \pi^+\pi^-$, and $D^0 \to K^-\pi^+$ decays. The values obtained from the two decay channels, KK and $\pi\pi$, are

$$y_{CP}^{KK} = (75.98 \pm 0.07\ ({\rm stat}) \pm 0.06\ ({\rm syst}))\,\%,$$

and

$$y_{CP}^{\pi\pi} = (76.29 \pm 0.14\ ({\rm stat}) \pm 0.05\ ({\rm syst}))\,\%.$$

The values are compatible within 1.8 standard deviations, and when combined they yield a final result of

$$y_{CP} = (76.08 \pm 0.06\ ({\rm stat}) \pm 0.04\ ({\rm syst}))\,\%,$$

in which the systematic uncertainty is still preliminary.

Conclusions

In this thesis a measurement of the charm-mixing observable y_{CP} was performed with $D^0 \to K^+K^-$, $D^0 \to \pi^+\pi^-$, and $D^0 \to K^-\pi^+$ decays where the D^0 meson originated from semileptonic B decays. The data sample, collected by LHCb with pp collisions at a centre-of-mass energy of 13 TeV, corresponds to an integrated luminosity of $5.57\,\text{fb}^{-1}$.

The analysis involves a fit to the ratio of $D^0 \to K^+K^-$ ($D^0 \to \pi^+\pi^-$) and $D^0 \to K^-\pi^+$ signal event yields as a function o the D^0 decay time to extract $\Delta\Gamma^{hh} = \Gamma_{h^+h^-} - \Gamma_{K^-\pi^+} = y_{CP}/\tau_{D^0}$, where h represents either a K or a π.

The results for the difference between the decay widths $\Delta\Gamma^{KK}$ and $\Delta\Gamma^{\pi\pi}$ are:

$$\Delta\Gamma^{KK} = (-1.8527 \pm 0.0021\ (\text{stat}) \pm 0.0011\ (\text{syst}))\,\text{ps}^{-1}$$
$$\Delta\Gamma^{\pi\pi} = (-1.8603 \pm 0.0036\ (\text{stat}) \pm 0.0014\ (\text{syst}))\,\text{ps}^{-1}.$$

Note that in this thesis the central values of $\Delta\Gamma$ and y_{CP} are blind, *i.e.* shifted by an unknown random value (the same shift is used for both the KK and $\pi\pi$ sample).

Using as input the precisely known value of the average D^0 lifetime, $\tau_{D^0} = (0.4101 \pm 0.0015)\,\text{ps}$, y_{CP} is determined from the two decay channels as

$$y_{CP}^{KK} = (75.98 \pm 0.07\ (\text{stat}) \pm 0.06\ (\text{syst}))\,\%$$
$$y_{CP}^{\pi\pi} = (76.29 \pm 0.14\ (\text{stat}) \pm 0.05\ (\text{syst}))\,\%.$$

The two values are consistent with each other, and when combined they give the final result with preliminary systematic uncertainties:

$$y_{CP} = (76.08 \pm 0.06\ (\text{stat}) \pm 0.04\ (\text{syst}))\,\%,$$

which is the most precise measurement of y_{CP} from a single experiment, and a factor of two better than the current world average $y_{CP} = (0.715 \pm 0.111)\,\%$.

When the analysis will reach a satisfying state, the unblinding of the central values will be performed, showing if the value of y_{CP} is consistent with the current world average of $y = \left(0.651^{+0.063}_{-0.069}\right)\,\%$; in case the values of the two observables are found to be incompatible, it would imply the observation of indirect CP violation in charmed mesons mixing.

Bibliography

[1] S. Chatrchyan, V. Khachatryan, et al. “Observation of a new boson at a mass of 125 GeV with the CMS experiment at the LHC”. In: *Physics Letters B* 716.1 (2012), pp. 30–61.

[2] G. Aad, T. Abajyan, et al. “Observation of a new particle in the search for the Standard Model Higgs boson with the ATLAS detector at the LHC”. In: *Physics Letters B* 716.1 (2012), pp. 1–29.

[3] S. L. Glashow. “Partial-symmetries of weak interactions”. In: *Nuc. Phys.* 22.4 (1961), pp. 579–588.

[4] S. Weinberg. “A Model of Leptons”. In: *Phys. Rev. Lett.* 19 (21 Nov. 1967), pp. 1264–1266.

[5] A. Salam. “Weak and Electromagnetic Interactions”. In: *Conf. Proc.* C680519 (1968), pp. 367–377.

[6] M. E. Peskin and D. V. Schroeder. *An Introduction to quantum field theory*. Addison-Wesley, 1995.

[7] Y. Fukuda, T. Hayakawa, et al. “Evidence for Oscillation of Atmospheric Neutrinos”. In: *Phys. Rev. Lett.* 81.8 (Aug. 1998), pp. 1562–1567.

[8] A. D. Sakharov. “Violation of *CP* Invariance, *C* asymmetry, and baryon asymmetry of the universe”. In: *Sov. Phys. Usp.* 34.5 (1991), pp. 392–393.

[9] M. Sozzi. *Discrete symmetries and CP violation: From experiment to theory*. Oxford University Press, 2008.

[10] T. D. Lee and C. N. Yang. “Question of Parity Conservation in Weak Interactions”. In: *Phys. Rev.* 104 (1 Oct. 1956), pp. 254–258.

[11] C. S. Wu, E. Ambler, et al. “Experimental Test of Parity Conservation in Beta Decay”. In: *Phys. Rev.* 105 (4 Feb. 1957), pp. 1413–1415.

[12] R. L. Garwin, L. M. Lederman, et al. “Observations of the Failure of Conservation of Parity and Charge Conjugation in Meson Decays: the Magnetic Moment of the Free Muon”. In: *Phys. Rev.* 105 (4 Feb. 1957), pp. 1415–1417.

[13] J. H. Christenson, J. W. Cronin, et al. “Evidence for the 2π Decay of the K_2^0 Meson”. In: *Phys. Rev. Lett.* 13 (4 June 1964), pp. 138–140.

[14] N. Cabibbo. “Unitary Symmetry and Leptonic Decays”. In: *Phys. Rev. Lett.* 10 (12 June 1963), pp. 531–533.

[15] M. Kobayashi and T. Maskawa. “CP-Violation in the Renormalizable Theory of Weak Interaction”. In: *Prog. Theor. Phys.* 49.2 (Feb. 1973), pp. 652–657.

[16] L. Wolfenstein. “Parametrization of the Kobayashi-Maskawa Matrix”. In: *Phys. Rev. Lett.* 51 (21 Nov. 1983), pp. 1945–1947.

[17] M. Tanabashi et al. “Review of Particle Physics”. In: *Phys. Rev. D* 98.3 (2018), p. 030001.

[18] C. Jarlskog. “Commutator of the Quark Mass Matrices in the Standard Electroweak Model and a Measure of Maximal CP Nonconservation”. In: *Phys. Rev. Lett.* 55 (10 Sept. 1985), pp. 1039–1042.

[19] I. I. Bigi and A. I. Sanda. *CP violation*. 2nd ed. Cambridge University Press, 2009.

[20] J. Charles, A. Höcker, et al. “CP violation and the CKM matrix: assessing the impact of the asymmetric B factories”. In: *Eur. Phys. J. C* 41.1 (May 2005), pp. 1–131. arXiv: `hep-ph/0406184`.

[21] Y. Nagashima. *Elementary Particle Physics. Volume 2: Foundations of the Standard Model*. John Wiley & Sons, 2013. ISBN: 978-3-527-40966-2.

[22] Y. S. Amhis, S. Banerjee, et al. *Averages of b-hadron, c-hadron, and τ-lepton properties as of 2018*. Updated results and plots available at `https://hflav.web.cern.ch/`. Sept. 2019. arXiv: `1909.12524 [hep-ex]`.

[23] J. H. Christenson, J. W. Cronin, et al. “Evidence for the 2π Decay of the K_2^0 Meson”. In: *Phys. Rev. Lett.* 13 (4 July 1964), pp. 138–140.

[24] B. Aubert, D. Boutigny, et al. “Observation of CP Violation in the B^0 Meson System”. In: *Phys. Rev. Lett.* 87 (9 Aug. 2001), p. 091801.

[25] K. Abe, K. Abe, et al. “Observation of Large CP Violation in the Neutral B Meson System”. In: *Phys. Rev. Lett.* 87 (9 Aug. 2001), p. 091802.

[26] R. Aaij, C. Abellán Beteta, et al. “First Observation of CP Violation in the Decays of B_s^0 Mesons”. In: *Phys. Rev. Lett.* 110 (22 May 2013), p. 221601.

[27] R. Aaij, C. Abellán Beteta, et al. "Observation of CP Violation in Charm Decays". In: *Phys. Rev. Lett.* 122 (21 May 2019), p. 211803.

[28] J. Lees, V. Poireau, et al. "Measurement of D^0-$\overline{D}^0$ Mixing and CP Violation in Two-Body D^0 Decays". In: *Phys. Rev. D* 87.1 (2013), p. 012004. arXiv: 1209.3896 [hep-ex].

[29] M. Starič, A. Abdesselam, et al. "Measurement of D^0-$\overline{D^0}$ mixing and search for CP violation in $D^0 \to K^+K^-, \pi^+\pi^-$ decays with the full Belle data set". In: *Phys. Lett. B* 753 (2016), pp. 412–418. arXiv: 1509.08266 [hep-ex].

[30] R. Aaij, C. Abellán Beteta, et al. "Measurement of the Charm-Mixing Parameter y_{CP}". In: *Phys. Rev. Lett.* 122 (1 Jan. 2019), p. 011802.

[31] L. Evans and P. Bryant. "LHC Machine". In: *JINST* 3.08 (Aug. 2008), S08001–S08001.

[32] J. Haffner. *The CERN accelerator complex. Complexe des accélérateurs du CERN*. General Photo. Oct. 2013. URL: https://cds.cern.ch/record/1621894.

[33] A. A. Alves, L. M. A. Filho, et al. "The LHCb Detector at the LHC". In: *JINST* 3.08 (Aug. 2008).

[34] A. A. Alves, L. M. A. Filho, et al. "LHCb detector performance". In: *Int. J. Mod. Phys. A* 30.07 (2015), p. 1530022.

[35] P. R. Barbosa-Marinho, I. Bediaga, et al. *LHCb VELO (VErtex LOcator): Technical Design Report*. Technical Design Report LHCb. Geneva: CERN, 2001.

[36] R. Aaij, A. Affolder, et al. "Performance of the LHCb Vertex Locator". In: *JINST* 9.09 (Sept. 2014), P09007–P09007.

[37] P. R. Barbosa-Marinho, I. Bediaga, et al. *LHCb inner tracker: Technical Design Report*. Technical Design Report LHCb. revised version number 1 submitted on 2002-11-13 14:14:34. Geneva: CERN, 2002.

[38] P. R. Barbosa-Marinho, I. Bediaga, et al. *LHCb outer tracker: Technical Design Report*. Technical Design Report LHCb. Geneva: CERN, 2001.

[39] S. Amato, D. Carvalho, et al. *LHCb magnet: Technical Design Report*. Technical Design Report LHCb. Geneva: CERN, 2000.

[40] S. Amato, D. Carvalho, et al. *LHCb RICH: Technical Design Report*. Technical Design Report LHCb. Geneva: CERN, 2000.

[41] M. Adinolfi, J. M. Kariuki, et al. *LHCb Upgraded RICH 1 Engineering Design Review Report*. Tech. rep. LHCb-PUB-2016-014. June 2016.

[42] S. Amato, D. Carvalho, et al. *LHCb calorimeters: Technical Design Report*. Technical Design Report LHCb. Geneva: CERN, 2000.

[43] R. Antunes-Nobrega, A. França-Barbosa, et al. *LHCb trigger system: Technical Design Report*. Technical Design Report LHCb. Geneva: CERN, 2003.

[44] R. Aaij, S. Amato, et al. "Tesla: An application for real-time data analysis in High Energy Physics". In: *Comput. Phys. Commun.* 208 (Nov. 2016), pp. 35–42.

[45] W. D. Hulsbergen. "Decay chain fitting with a Kalman filter". In: *Nuc. Instrum. Meth.* 552.3 (Nov. 2005), pp. 566–575.

[46] R. Aaij, B. Adeva, et al. "Measurement of B_s^0 and D_s^- Meson Lifetimes". In: *Phys. Rev. Lett.* 119 (10 Sept. 2017), p. 101801.

Appendix A

Fits to the D^0 mass

In this appendix the details of the fit to the D^0 mass distribution to estimate the signal yields are reported. For a description of the fit model and procedure, see Sect. 3.3.

The fits to the MC samples are shown in Fig. A.1, while the fit parameters are reported in Tab. A.1. In Figs. A.2 to A.4 the mass fits in each decay-time bin for the $D^0 \to K^+K^-$, $D^0 \to \pi^+\pi^-$, and $D^0 \to K^-\pi^+$ decay channels are shown, with their signal yields reported in Tab. A.2.

Table A.1: Parameters of the fit to the D^0 mass distribution from the MC sample.

Parameter	Fit values		
	KK	$K\pi$	$\pi\pi$
N_{sig}	8298814 ± 2871	34172434 ± 5845	4050293 ± 2012
c_1	0.5276 ± 0.0078	0.5059 ± 0.0056	0.417 ± 0.012
c_2	0.1950 ± 0.0065	0.03735 ± 0.00094	0.101 ± 0.011
c_3	0.0273 ± 0.0017	0.2284 ± 0.0084	
μ_1 [MeV/c^2]	1866.1031 ± 0.0096	1866.3161 ± 0.0076	1866.039 ± 0.097
k_2	1.648 ± 0.022	4.337 ± 0.082	2.460 ± 0.037
k_3	4.81 ± 0.14	1.655 ± 0.013	0.6381 ± 0.0034
k_4	0.6974 ± 0.0025	0.6954 ± 0.0024	
δ_2 [MeV/c^2]	0.558 ± 0.075	-1.809 ± 0.79	-7.25 ± 1.6
δ_3 [MeV/c^2]	12.5 ± 1.9	-0.4006 ± 0.052	0.448 ± 0.092
δ_4 [MeV/c^2]	-0.0367 ± 0.018	-0.0719 ± 0.013	
σ_1 [MeV/c^2]	6.890 ± 0.020	7.985 ± 0.039	10.38 ± 0.11
s	0.99205 ± 0.00026	0.98786 ± 0.00026	0.9894 ± 0.0032

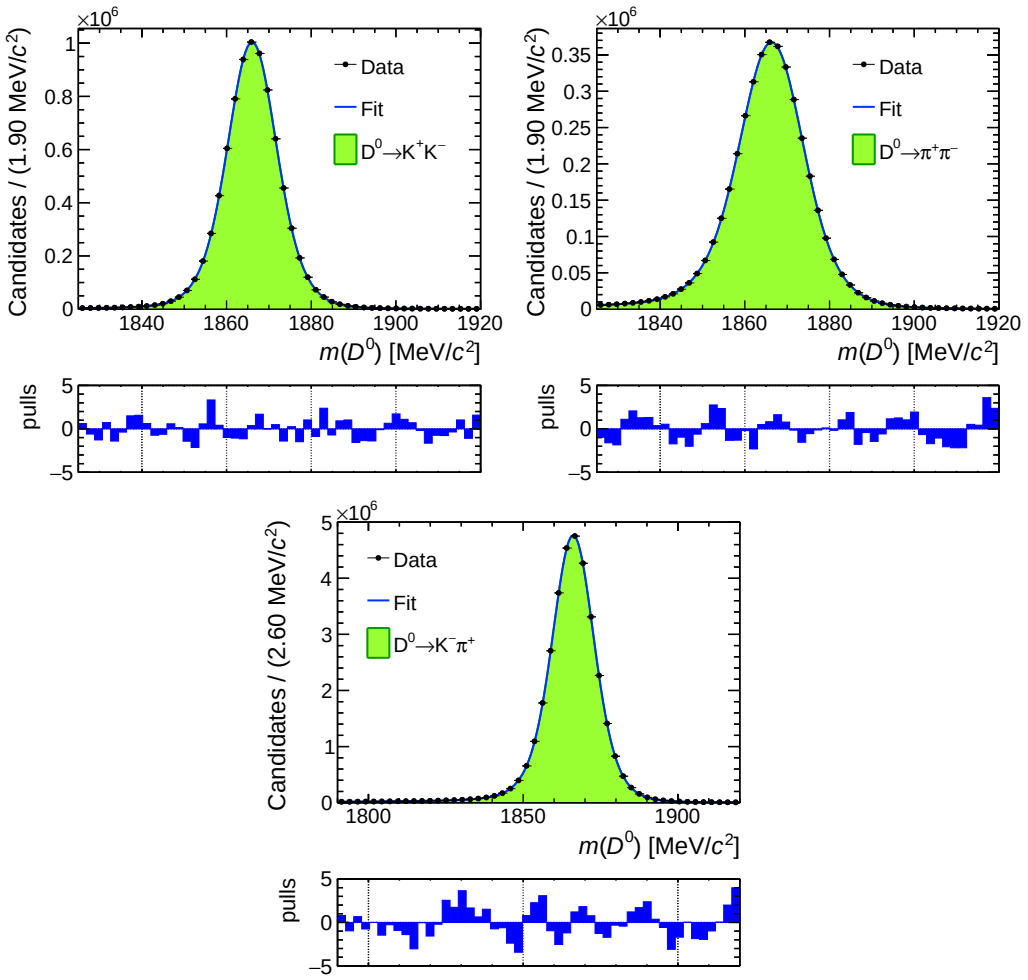

Figure A.1: Fits to the simulated $m(D^0)$ samples, in the $D^0 \to K^+K^-$ (top left), $D^0 \to \pi^+\pi^-$ (top right), and $D^0 \to K^-\pi^+$ (bottom) decay channel.

Table A.2: Signal yields from the fits to the D^0 mass distribution in each D^0 decay-time bin.

Bin edges	Signal yields		
[ps]	$K\pi$	KK	$\pi\pi$
0.15-0.20	3381099 ± 1907	356703 ± 681	128583 ± 480
0.20-0.24	2525693 ± 1647	265485 ± 585	96076 ± 402
0.24-0.30	3456036 ± 1926	365021 ± 683	129740 ± 460
0.30-0.35	2570590 ± 1661	271559 ± 586	96735 ± 390
0.35-0.41	2737511 ± 1714	289031 ± 602	102543 ± 396
0.41-0.74	2395921 ± 1604	252865 ± 561	89346 ± 367
0.47-0.54	2411842 ± 1608	253897 ± 560	90134 ± 366
0.54-0.60	1777045 ± 1380	187497 ± 480	66565 ± 313
0.60-0.68	2008181 ± 1468	210959 ± 508	75482 ± 333
0.68-0.76	1664782 ± 1337	175367 ± 462	61053 ± 301
0.76-0.84	1376639 ± 1215	144416 ± 419	50712 ± 274
0.84-0.94	1387009 ± 1220	145499 ± 419	51039 ± 274
0.94-1.04	1092228 ± 1083	115115 ± 373	40365 ± 247
1.04-1.16	1007315 ± 1040	105488 ± 357	37111 ± 238
1.16-1.29	809187 ± 932	84628 ± 320	30112 ± 217
1.29-1.44	664109 ± 845	69918 ± 291	24656 ± 199
1.44-1.63	560958 ± 777	58499 ± 267	20632 ± 185
1.63-1.95	518595 ± 749	54008 ± 258	19000 ± 187

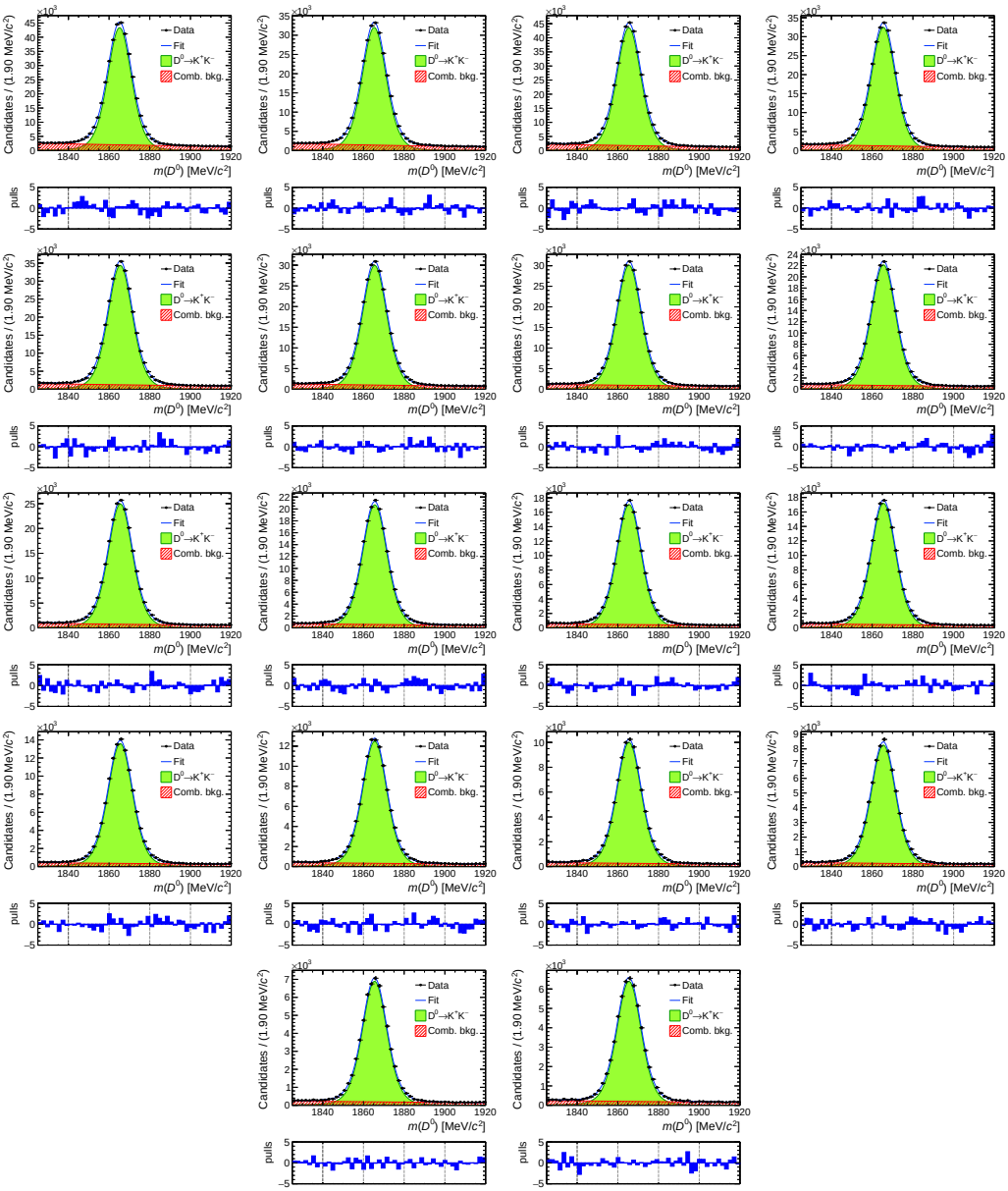

Figure A.2: Fits to the $D^0 \to K^+K^-$ mass in each decay-time bin, in increasing order from left to right and from top to bottom.

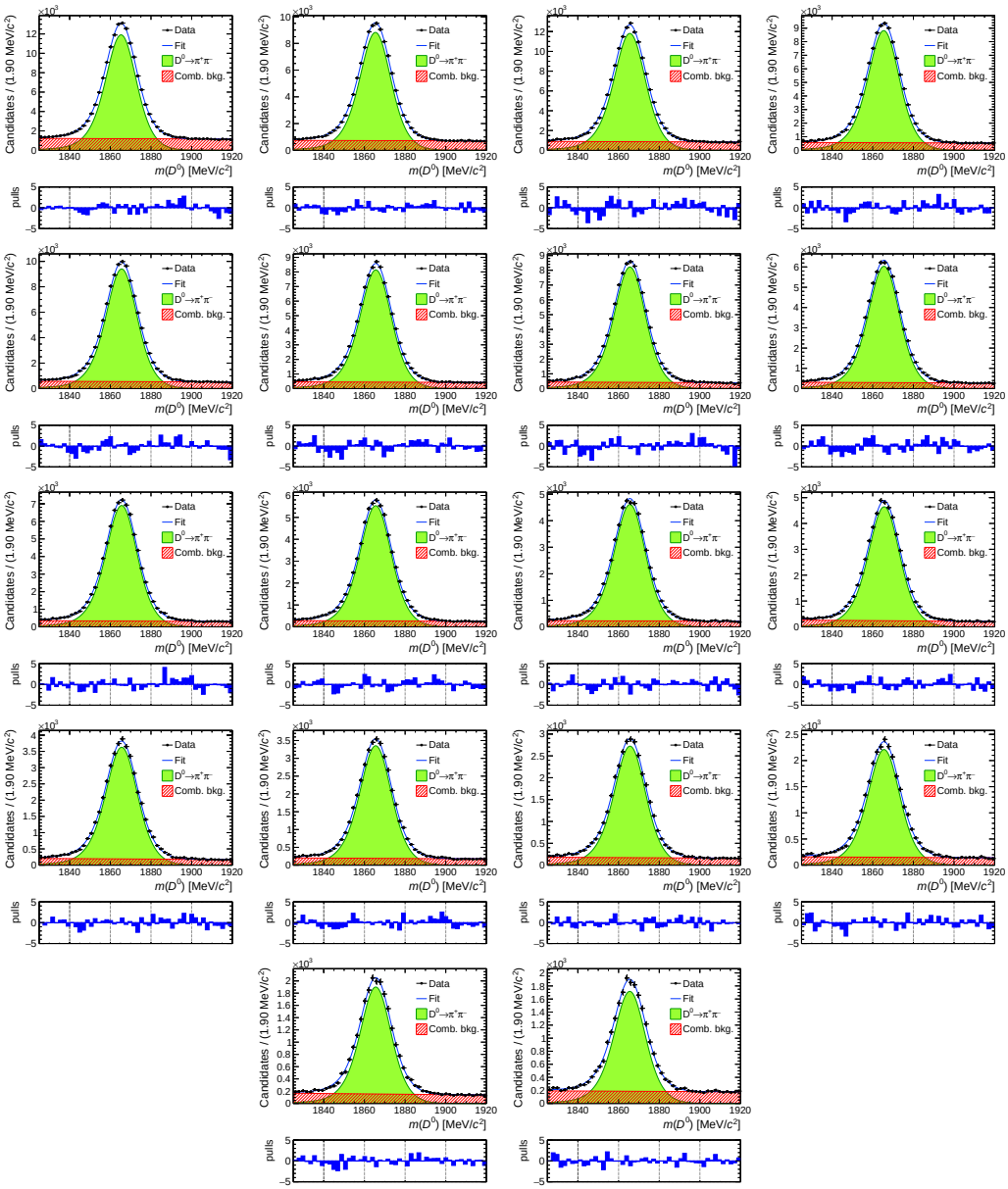

Figure A.3: Fits to the $D^0 \to \pi^+\pi^-$ mass in each decay-time bin, in increasing order from left to right and from top to bottom.

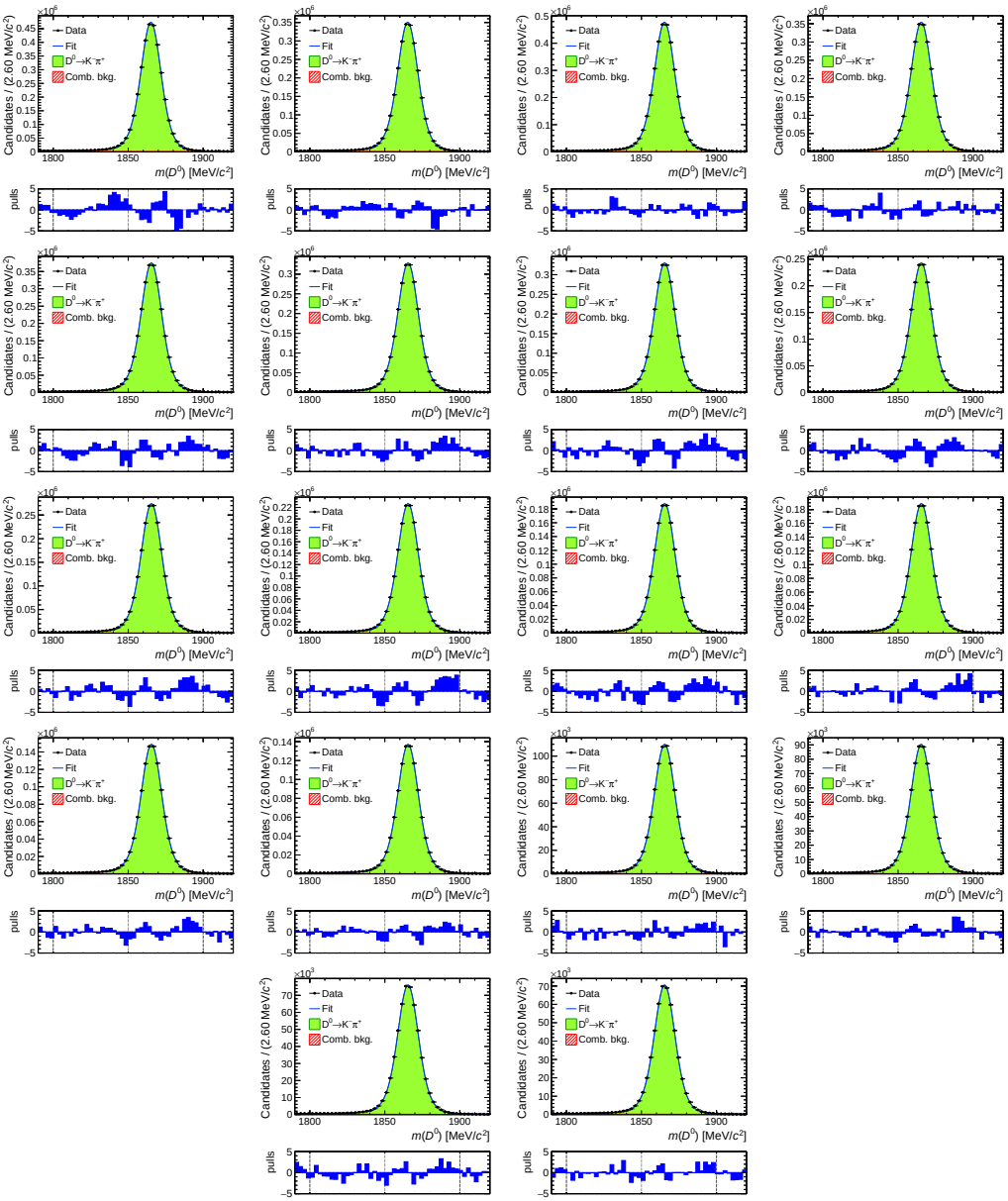

Figure A.4: Fits to the $D^0 \to K^-\pi^+$ mass in each decay-time bin, in increasing order from left to right and from top to bottom.